A singular plasmonic-thermoelectric hollow nanostructure inducing apoptosis and cuproptosis for catalytic cancer therapy

Lu Yang[1,2,5], Zhiyu Zhao[3,5], Boshi Tian[1], Meiqi Yang[1], Yushan Dong [1], Bingchen Zhou[1], Shili Gai [1] ✉, Ying Xie [4] ✉ & Jun Lin [2] ✉

Thermoelectric technology has recently emerged as a distinct therapeutic modality. However, its therapeutic effectiveness is significantly limited by the restricted temperature gradient within living organisms. In this study, we introduce a high-performance plasmonic-thermoelectric catalytic therapy utilizing urchin-like $Cu_{2-x}Se$ hollow nanospheres (HNSs) with a cascade of plasmonic photothermal and thermoelectric conversion processes. Under irradiation by a 1064 nm laser, the plasmonic absorption of $Cu_{2-x}Se$ HNSs, featuring rich copper vacancies (V_{Cu}), leads to a rapid localized temperature gradient due to their exceptionally high photothermal conversion efficiency (67.0%). This temperature gradient activates thermoelectric catalysis, generating toxic reactive oxygen species (ROS) targeted at cancer cells. Density functional theory calculations reveal that this vacancy-enhanced thermoelectric catalytic effect arises from a much more carrier concentration and higher electrical conductivity. Furthermore, the exceptional photothermal performance of $Cu_{2-x}Se$ HNSs enhances their peroxidase-like and catalase-like activities, resulting in increased ROS production and apoptosis induction in cancer cells. Here we show that the accumulation of copper ions within cancer cells triggers cuproptosis through toxic mitochondrial protein aggregation, creating a synergistic therapeutic effect. Tumor-bearing female BALB/c mice are used to evaluate the high anti-cancer efficiency. This innovative approach represents the promising instance of plasmonic-thermoelectric catalytic therapy, employing dual pathways (membrane potential reduction and thioctylated protein aggregation) of mitochondrial dysfunction, all achieved within a singular nanostructure. These findings hold significant promise for inspiring the development of energy-converting nanomedicines.

Thermoelectric catalytic therapy (TECT) is an emerging therapeutic approach that relies on the conversion of thermal energy to electricity *via* a temperature gradient, activating reactive oxygen species (ROS)-enabled catalytic therapy[1,2]. This temperature gradient in thermoelectric materials induces electron-hole (e^--h^+) separation and generates a built-in electric field[3–5], initiating a redox reaction to produce ROS for therapeutic purposes[6,7]. However, TECT faces challenges in the biomedical field due to limited temperature variations in living organisms, resulting in poor TECT, which is still in the initial stage in the biomedical field, because the limited temperature variations in

living organisms induce a low separation efficiency of e⁻-h⁺ in thermoelectric material[8–10], and consequently, inadequate ROS generation and therapeutic efficacy[11]. Hence, it is imperative to develop a localized heat source that only heats the thermoelectric material to achieve a satisfactory effect.

To address these limitations, leveraging photothermal-activated thermoelectric effects to increase temperature variations at tumor sites offers a promising solution. Although some studies have explored this approach using materials such as Bi_2Te_3 nanoplates, $Bi_{0.5}Sb_{1.5}Te_3$/ CaO_2 nanosheets, $Bi_{0.5}Sb_{1.5}Te_3$/$Bi_2Te_{2.8}Se_{0.2}$ heterojunctions, rGO-Bi_2Te_3 nanosheets, and Ag-Ag_2S nanoparticles[1,2,6,11,12], these materials often involve complex compositions/structures and suffer from low synthesis repeatability, posing challenges in biocompatibility and safety[13–15]. In addition, the limited temperature gradient persists due to the low photothermal conversion efficiency ~16%–34%, even with these complex materials. Therefore, there is a pressing need to develop simpler structures and more effective heating strategies.

Plasmonic nanostructures, capable of absorbing and converting light into heat, offer a promising solution for generating localized heat efficiently[16–19]. Plasmonic heat can be dynamically controlled by external light irradiation, making it a versatile, fast, and controllable localized heat source[20,21]. Plasmonic nanostructures can significantly enhance light absorption by confining light within the nanostructure. This approach has the advantage of wavelength- or polarization-sensitive absorption, allowing control of light absorption by tuning the structural parameters of the nanostructures[22]. Plasmonic photo-thermoelectric conversion, as an energy conversion modality, can significantly enhance thermoelectric efficacy[23,24]. Enhanced thermoelectric response using plasma thermal effects has been studied in the thermoelectric field. Studies of photo-thermoelectric detectors incorporating plasma absorbers have shown that plasma can enhance the sensitivity of thermoelectric devices[16,22]. To realize such energy transfer, the current approach is strongly reliant on the combination of plasmonic and thermoelectric materials, such as hybrids of Pt/CoFeB, Au-Si/Bi_2Te_3, and Ag/PEDOT:PSS[16,22,25]. However, it is challenging to achieve plasmonic thermoelectric effects in a single material to avoid biosafety issues caused by material complexity[26]. Research on plasmonic thermoelectric therapy is still lacking. In particular, an in-depth understanding of the regulation and alteration of the internal structure, such as the introduction of vacancies in a single material, may help improve the plasmonic photothermal and thermoelectric performances.

Cu_2Se, an exceptional thermoelectric material, has garnered considerable attention due to its non-toxic nature and wide operational temperature range[27,28]. Importantly, the existence of abundant copper vacancies (V_{Cu}) has offered a viable approach to enhance Cu_2Se through the formation of non-stoichiometric $Cu_{2-x}Se$. This process can optimize thermoelectric properties and induce strong plasmonic absorption[29,30]. V_{Cu} can improve the plasma absorption effect by altering the electronic structure and optical properties of the material. First, vacancies introduce defects in the material, and these defects can alter the electronic structure of the material, which contributes to enhancing the plasma absorption of the material within a specific wavelength range[31]. Second, the defect regions formed by vacancies in the material may produce localized electric field enhancement effects, thereby enhancing the efficiency of plasma absorption[32]. Third, vacancies may act as scattering centers, increasing the propagation path and scattering number of light in the material, thereby enhancing the light absorption efficiency[33]. Consequently, $Cu_{2-x}Se$ represents an ideal thermoelectric material for facilitating energy conversion *via* the plasmonic photothermal effect combined thermoelectricity pathway. In particular, vacancy-triggered plasmonic absorption is located in the near-infrared II (NIR-II, 1000–1700 nm) region, which has centimeter tissue penetration with reduced light scattering[34–37], thus enabling the remote control of located heating and initiating excellent thermoelectric effects in tissues. This suggests that $Cu_{2-x}Se$ has the potential to achieve NIR-II light-activated plasmonic TECT. Furthermore, $Cu_{2-x}Se$ is a suitable copper carrier, which can result in the accumulation of copper in cancer cells, leading to a special form of programmed cell death of cuproptosis through copper-dependent mitochondrial dysfunction[38,39]. What's more, selenium is a necessary trace element for the human body and plays a crucial role in many physiological processes to maintain health[40]. Inorganic selenium contained in nanoparticles shows a cytotoxic effect, which can directly kill tumor cells and inhibit their aberrant proliferation. Inorganic selenium also exhibits a differentiation-promoting effect on tumor cells, which can reduce the invasiveness of tumors and ameliorate the prognosis of patients. Therefore, inorganic selenium is a promising and inexpensive antitumor agent with multiple antitumor effect[41,42]. It is thereby clear that $Cu_{2-x}Se$ is a good choice to achieve efficient curative effects by taking advantage of multimodal treatment strategies. However, aside from its intensive reports as a photothermal agent[43–45], the study of $Cu_{2-x}Se$ for TECT and its therapeutic mechanism is still limited.

Here, we show a comprehensive strategy utilizing V_{Cu}-enriched $Cu_{2-x}Se$ hollow nanospheres (HNSs), to simultaneously achieve plasmonic photothermal therapy, TECT, heat-enhanced enzymatic catalytic therapy, cuproptosis, and apoptosis in a single material mediated by NIR-II light (Fig. 1). Motivated by the improved cellular uptake and intratumoral accumulation associated with nanostructures possessing biomimetic morphology[46–48], urchin-like $Cu_{2-x}Se$ HNSs with spiky protrusions are purposefully designed. Under 1064 nm irradiation, the presence of V_{Cu} in $Cu_{2-x}Se$ HNSs exhibits strong plasmonic absorption capabilities and exceptionally high photothermal conversion efficiency (67%). This characteristic imparts $Cu_{2-x}Se$ HNSs with the ability to rapidly generate localized heating. Notably, this localized heating can serve as an excitation source for triggering TECT in $Cu_{2-x}Se$ HNSs, thereby enhancing their peroxidase (POD)-like and catalase (CAT)-like activities. Consequently, this process yields substantial amounts of ROS for highly effective therapeutic applications. Moreover, density functional theory (DFT) calculations employing the BoltzTrap code reveal that the vacancies in $Cu_{2-x}Se$ HNSs significantly contribute to the exceptional enzymatic and thermoelectric catalytic activities observed. Upon internalization of $Cu_{2-x}Se$ HNSs by cells, copper ions accumulate within the cellular environment. When combined with the ROS and heat generated, this accumulation triggers a dual mechanism involving cuproptosis and apoptosis, ultimately leading to the destruction of cancer cells.

Results
Characterization and properties
The basic characterization of Cu_2O and $Cu_{2-x}Se$ HNSs samples is summarized in Fig. 2. First, the synthesis mechanism of urchin-like $Cu_{2-x}Se$ HNSs through the Kirkendall effect is illustrated in Fig. 2a. As a sacrificial template, Cu_2O nanoparticles (NPs) were prepared by the reduction reaction of $Cu(OH)_2$ using sodium ascorbate. When the sacrificial template of Cu_2O is dispersed into a Se^{2-} solution, a $Cu_{2-x}Se$ thin layer would form on the surface of Cu_2O NPs. As the inward transport rate of Se^{2-} ions is slower than the outward transport rate of the copper ions through the formed $Cu_{2-x}Se$ thin layer, Kirkendall voids may form, thus, $Cu_{2-x}Se$ HNSs will be prepared[49,50]. The transmission electron microscopy (TEM) image in Fig. 2b shows the cubic morphology of the Cu_2O NPs with an average size of 95 nm. According to the Kirkendall effect, a $Cu_{2-x}Se$ hollow structure will be formed, just like the urchin-like nanosphere of 130 nm size exhibited in Fig. 2c. To obtain more structural information, high-resolution TEM (HRTEM) of $Cu_{2-x}Se$ HNSs was used to determine the interplanar distances between adjacent lattice fringes. The distance was 0.33 nm (Fig. 2d), which corresponds to the d_{111} spacing of $Cu_{2-x}Se$ (JCPDS No. 88-2043). The inset in Fig. 2d shows the corresponding selected area electron diffraction (SAED) pattern, revealing distinct diffraction spots at (111), (220), (311), (400), and (422). Notably, the elongated dot-like
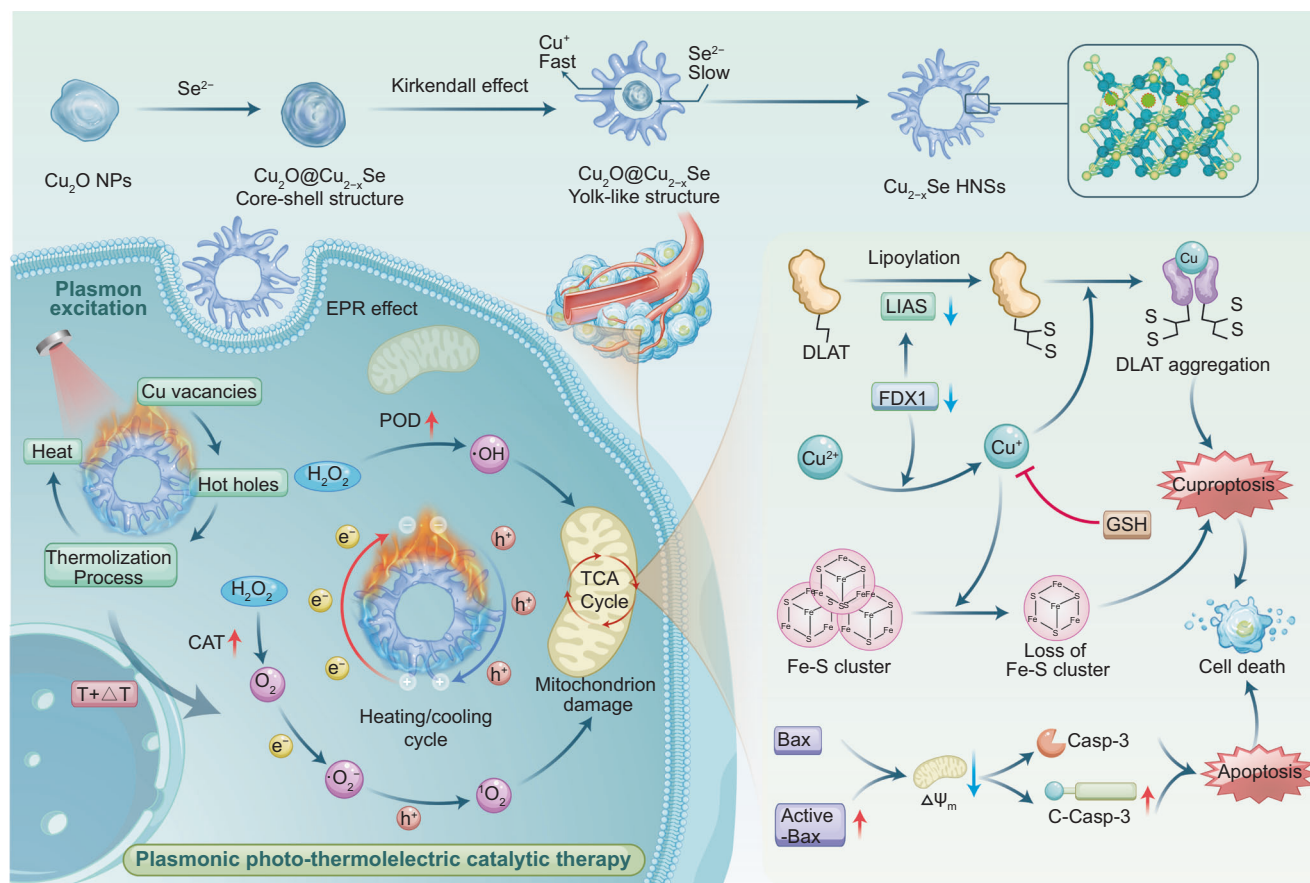
Fig. 1 | Synthesis process and therapeutic mechanim. Illustration of the synthesis process of $Cu_{2-x}Se$ HNSs, and anti-tumor process inducing cuproptosis and apoptosis activated by synergistic photothermal, enzymatic, and plasmonic thermoelectric catalysis therapies.

diffraction patterns do not conform to typical single-crystal dots or polycrystal rings, suggesting that $Cu_{2-x}Se$ HNSs exhibit a polycrystalline nature with small grains and low crystallinity. High-angle annular dark-field scanning transmission electron microscopy (HAADF-STEM) and the corresponding elemental mapping confirmed the uniform distribution of Cu and Se (Fig. 2e). In addition, a hollow structure was observed (Supplementary Fig. 1a). Besides, spherical $Cu_{2-x}Se$ ($Cu_{2-x}Se$ (sp)) was prepared to compare the performance, and the TEM image was shown in Supplementary Fig. 1b.

The phase transition from Cu_2O to $Cu_{2-x}Se$ was characterized *via* X-ray diffraction (XRD) (Fig. 2f). All the diffraction peaks of the synthesized Cu_2O samples coincided with the standard characteristic peaks of pure cubic Cu_2O (JCPDS No. 99-0041). For $Cu_{2-x}Se$ HNSs, all the diffraction peaks could be readily indexed to cubic berzelianite (Cu_2Se, Fm3m space group, JCPDS No. 88-2043), indicating that the existence of V_{Cu} does not change the crystal phase of Cu_2Se. Furthermore, no additional peaks for other phases associated were observed, indicating a high purity of $Cu_{2-x}Se$, and the complete conversion of Cu_2O to $Cu_{2-x}Se$. Thus, the crystal structure of $Cu_{2-x}Se$ is shown in Fig. 2g, and the positions of V_{Cu} are marked. The presence of Cu and Se in the sample was further confirmed *via* energy-dispersive X-ray spectroscopy (EDS), as depicted in Fig. 2h. The surface composition and chemical state of $Cu_{2-x}Se$ HNSs were analyzed using X-ray photoelectron spectroscopy (XPS) and the elemental compositions of Cu and Se were determined from the survey XPS spectrum (Fig. 2i). The high-resolution Cu 2p shows peaks at 932.05, 951.85, 933.66, and 953.43 eV, which were assigned to Cu $2p_{1/2}$ and Cu $2p_{3/2}$, respectively (Fig. 2j). Based on the integrated peak area ratio, the percentages of Cu^+ and Cu^{2+} were estimated to be 71.6% and 28.4%, respectively. The coexistence of Cu^+ and Cu^{2+} confirmed the successful preparation of

non-stoichiometric $Cu_{2-x}Se$ crystalline and the formation of V_{Cu}. In addition, the peaks at 54.3 and 53.4 eV in the Se 3d spectrum corresponded to Se $3d_{3/2}$ and Se $3d_{5/2}$, respectively (Fig. 2k)[43,51].

$Cu_{2-x}Se$ HNSs maintained a consistent hydrodynamic size when immersed in various physiological solutions of phosphate buffer solution (PBS), H_2O, saline, and medium, for incubation at different times (8, 16, 24, 48, and 72 h) as determined by dynamic light scattering (DLS) measurements (Supplementary Fig. 2). Furthermore, these HNSs exhibited stability for at least 72 h in PBS at pH 5.5, which simulates the internal tumor environment. This stability is advantageous for preserving catalytic properties in vivo. This is conducive to sustaining the catalytic properties in vivo. Need to mention, Cu ion release in the tumor microenvironment is a key indicator for triggering cuproptosis, we examined the level of Cu ion release from HNSs cultured at different times in different simulated environments as shown in Supplementary Fig. 3. Obviously, the high level of Cu ion release ensured effective cuproptosis. Glutathione (GSH), an endogenous antioxidant, plays a role in maintaining cellular redox homeostasis and inhibiting ROS-induced cellular damage through enzymatic catalysis, thermoelectric catalysis, and ROS-induced apoptosis mechanisms. Consequently, the reduction of GSH levels is crucial for enhancing treatment effectiveness. The impact of $Cu_{2-x}Se$ HNSs on GSH depletion was assessed using UV-vis spectrophotometry, as presented in Supplementary Fig. 4a. The GSH content exhibited a continuous decline with increasing exposure time to $Cu_{2-x}Se$ HNSs. These results underscore the potential of $Cu_{2-x}Se$ HNSs in the field of tumor therapy.

Plasmonic photothermal performance

The photothermal mechanism and performance of plasmonic $Cu_{2-x}Se$ HNSs, when irradiated by a 1064 nm laser, are shown in Fig. 3. Figure 3a
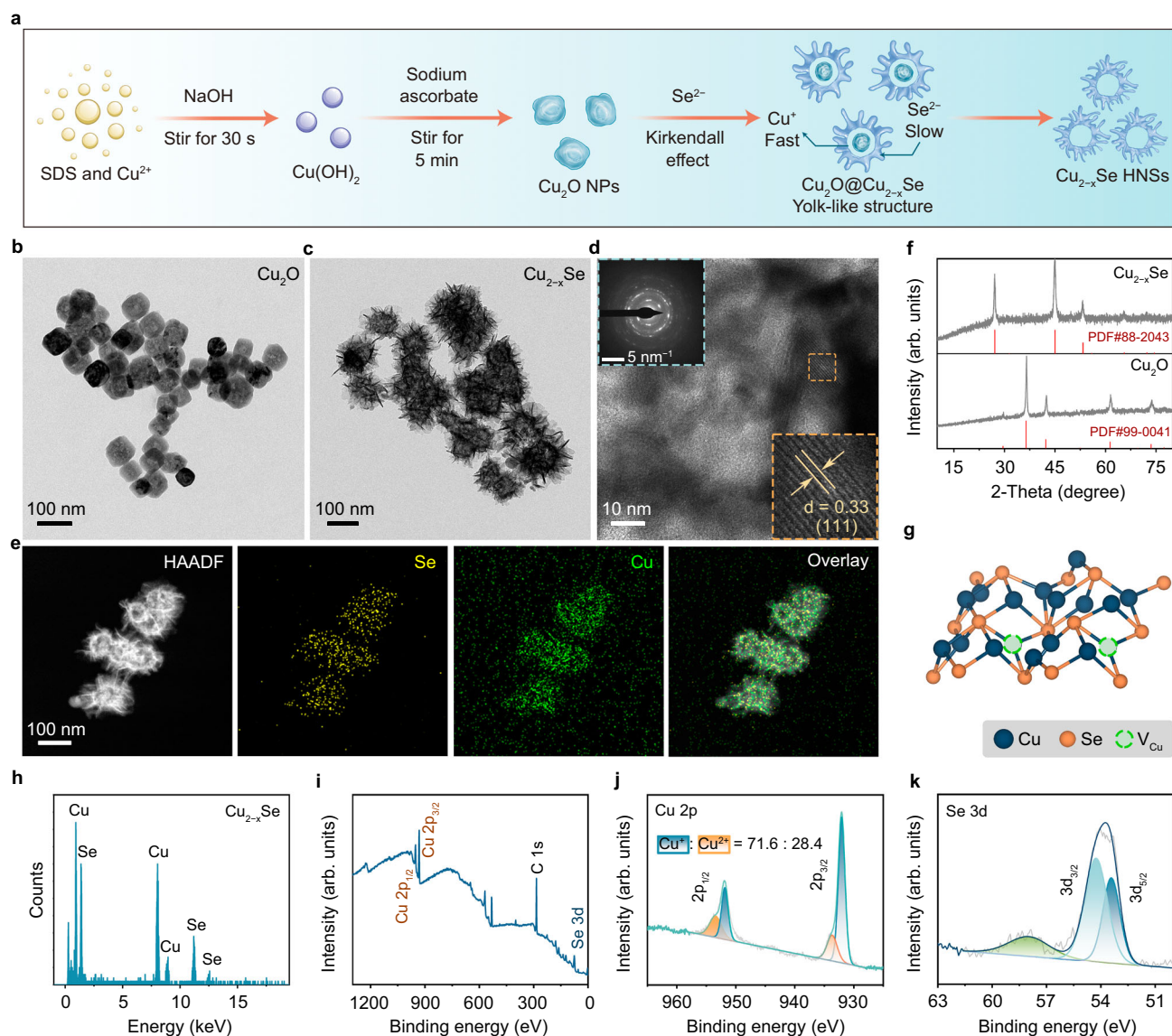
Fig. 2 | Basic characterization of Cu₂O and Cu₂₋ₓSe HNSs samples. a Schematic illustrating the synthesis process of Cu₂₋ₓSe HNSs. **b, c** TEM images of Cu₂O NPs and Cu₂₋ₓSe HNSs. **d** HRTEM image of Cu₂₋ₓSe HNSs. Inset: SAED pattern. **e** HAADF-STEM and corresponding elemental mapping of Cu₂₋ₓSe HNSs. **f** XRD spectra. **g** Crystal structure of Cu₂₋ₓSe HNSs. **h** EDS survey spectrum. **i–k** Survey XPS spectrum of Cu₂₋ₓSe HNSs (**i**), high-resolution XPS spectra of (**j**) Cu 2p and (**k**) Se 3d. Source data are provided as a Source Data file (arb. units, arbitrary units).

provides a schematic illustrating the photothermal mechanism of Cu₂₋ₓSe HNSs originating from plasmonic absorption. Plasmons are supported by positively charged holes generated by the presence of V_{Cu} in non-stoichiometric Cu₂₋ₓSe HNSs, typically with a carrier density ranging from 10^{19} to 10^{21} cm^{-3} [29,30]. Due to the abundance of V_{Cu}, Cu₂₋ₓSe HNSs possess a high concentration of free holes in the valence band (VB) structure. Upon plasmon photoexcitation, these hot holes become mobile[52]. These hot holes, upon thermalization processes, generate heat within Cu₂₋ₓSe HNSs and create a temperature gradient. Simultaneously, energy conversion occurs in thermoelectric Cu₂₋ₓSe HNSs, initiating the conversion of photothermal effect, thermoelectricity, and ROS, thereby achieving thermoelectric catalysis. Furthermore, the thermal effect can enhance the enzymatic activity of Cu₂₋ₓSe HNSs. Figure 3b shows strong and characteristic plasmonic absorption of Cu₂₋ₓSe HNSs in the NIR spectral region, particularly in the NIR-II transparent bio-window. The strong absorbance in the NIR-II region is significant for biomedical applications because NIR-II light, such as that at a wavelength of 1064 nm, experiences less scattering in biological tissues, allowing for deeper penetration into tissues.

To verify the photothermal performance, both the extinction coefficient (ε) and photothermal conversion efficiency (η) of Cu₂₋ₓSe HNSs were evaluated. The absorbance of a Cu₂₋ₓSe HNSs solution was used to determine the normalized adsorption intensity over the length of the cell (A/L) at 1064 nm with varying concentrations, as shown in Fig. 3b. Utilizing the Lambert-Beer law, the ε at 1064 nm was calculated to be 1.52 L g^{-1} cm^{-1}, as demonstrated in Fig. 3c. In Fig. 3d, it can be seen that the increased temperature of the Cu₂₋ₓSe HNSs solution exhibits a dependence on the power density, as the laser power shows a positive correlation with the heating rate. Figure 3e shows the temperature variation curves for different concentrations of Cu₂₋ₓSe HNSs solution and water, and typical infrared thermal images are presented in Fig. 3f. The temperature of the Cu₂₋ₓSe HNSs solution at a concentration of 80 µg mL^{-1} can rise from 21.0 °C to 73.8 °C in 5 min under 1.0 W cm^{-2} laser irradiation, while the temperature variation for pure water was less than 5.0 °C under the same conditions, indicating that the thermal energy was converted by Cu₂₋ₓSe HNSs rapidly. Thus, a photoinduced temperature increase is an excellent excitation source for the initiation of thermoelectric catalysis. The concentration- and power-dependent
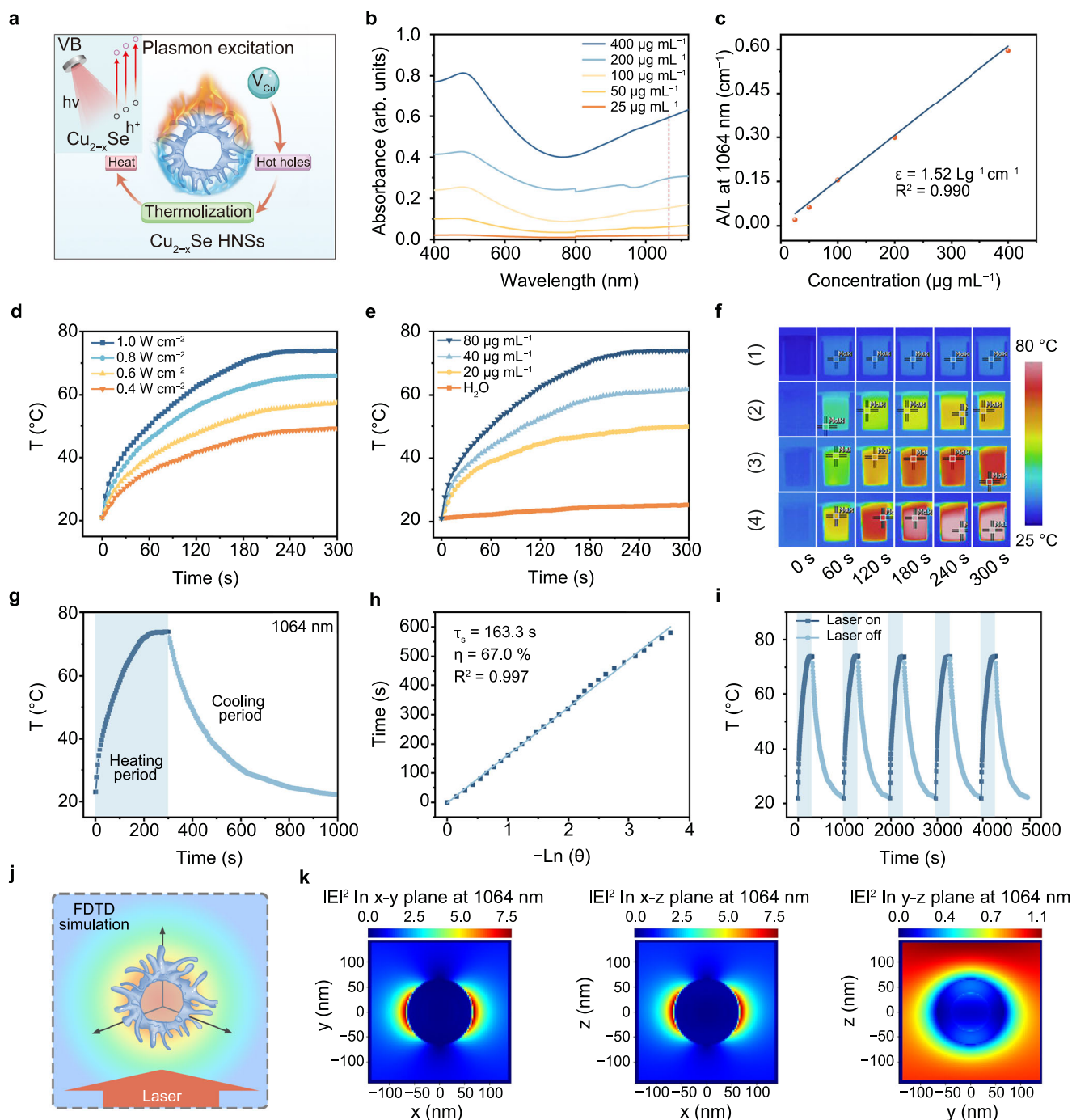
Fig. 3 | Photothermal mechanism and performance of plasmonic $Cu_{2-x}Se$ HNSs irradiated by 1064 nm laser (1.0 W cm^{-2}). **a** Schematic illustration of the photothermal mechanism of $Cu_{2-x}Se$ HNSs originating from plasmonic absorption. **b** UV-vis absorption spectra of $Cu_{2-x}Se$ HNSs at varied concentrations. **c** Mass extinction coefficient fitting curve of $Cu_{2-x}Se$ HNSs at 1064 nm. **d, e** Power-dependent (**d**) and concentration-dependent (**e**) heating curves of $Cu_{2-x}Se$ HNSs solution irradiated by laser for 5 min. **f** Infrared thermal images of $Cu_{2-x}Se$ HNSs solutions with concentrations of (1) 0, (2) 20, (3) 40, and (4) 80 μg mL^{-1}. **g** Photothermal heating curve of $Cu_{2-x}Se$ HNSs solution irradiated with laser for 5 min and cooling curve after switching off the laser. **h** Linear relationship between $-\mathrm{Ln}\theta$ and time during the cooling period. **i** Heating curves of $Cu_{2-x}Se$ HNSs aqueous solutions for five laser on/off cycles under laser irradiation. **j** Schematic illustration of the 3D-FDTD simulation around the $Cu_{2-x}Se$ HNSs at a specific incident wavelength of 1064 nm. **k** 3D-FDTD simulated spatial distribution of the electric field. Source data are provided as a Source Data file (arb. units, arbitrary units).

temperature variation confirms an efficient controllability of the photothermal effect of $Cu_{2-x}Se$ HNSs. Derived from the cooling period in Fig. 3g, the time constant (τ_s) of $Cu_{2-x}Se$ HNSs was determined to be 163.3 s (Fig. 3h), and the η under 1064 nm irradiation is ~ 67.0%. The results demonstrate the excellent photothermal performance of $Cu_{2-x}Se$ HNSs under NIR-II laser irradiation owing to the strong plasmonic absorption in the NIR-II region resulting from the V_{Cu}.

Finally, the key parameter of photothermal stability was assessed (Fig. 3i). $Cu_{2-x}Se$ HNSs showed excellent photothermal stability with negligible attenuation of temperature after five heating/cooling cycles. In addition, three-dimensional finite-difference time-domain (3D-FDTD) simulations were performed to obtain the electric field distribution of $Cu_{2-x}Se$ HNSs (Fig. 3j). The profiles of the electric field (described by $|E|^2$) were simulated as a function of
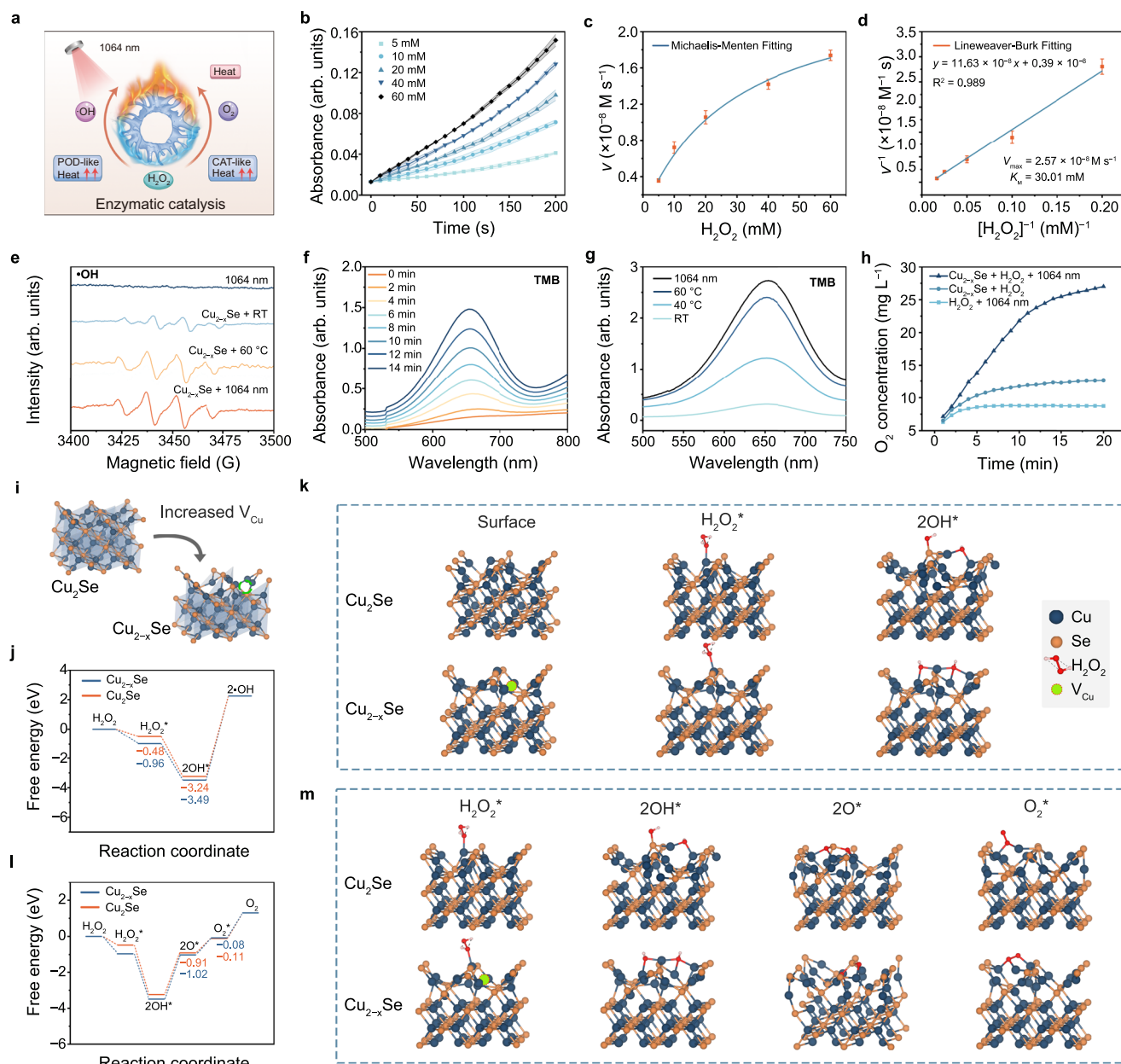
Fig. 4 | Assessment of enzymatic catalysis activity and mechanism. a Enzymatic catalysis mechanism diagram. **b** Absorbance of oxTMB at 652 nm in $Cu_{2-x}Se$ HNSs solutions with different concentrations of H_2O_2 over time. **c, d** Michaelis-Menten kinetic analysis (**c**) and Lineweaver-Burk plot (**d**). Data presented as mean ± S.D. (*n* = 3 independent data). **e** ESR spectra of ·OH trapped by DMPO in $Cu_{2-x}Se$ HNSs and H_2O_2 mixed solution (Heating and 1064 nm irradiation time: 5 min; 1064 nm irradiation power: 1.0 W cm^{-2}). **f, g** UV-vis absorption spectra of oxTMB in $Cu_{2-x}Se$ HNSs and H_2O_2 solution versus standing time (**f**) and temperatures (**g**). **h** O_2 generation curves under different conditions. **i** Schematic models of the Cu_2Se and $Cu_{2-x}Se$ with Cu vacancies. **j**–**m** Energy profiles of the POD-like (**j**) and CAT-like (**l**) catalytic pathways for Cu_2Se and $Cu_{2-x}Se$ surfaces, and corresponding optimized structures (**k**, **m**). Source data are provided as a Source Data file (arb. units, arbitrary units).

the 1064 nm incident wavelength along the *z*-direction. In Fig. 3k, remarkable electric field enhancement is shown on two sides of the $Cu_{2-x}Se$ HNSs with an $|E|^2$ value of about 7.5, demonstrating an intense interaction with the 1064 nm external light. According to the results of FDTD, theoretically, 1064 nm is located in the plasmonic excitation wavelength range of $Cu_{2-x}Se$ HNSs and thus can be used as an excitation source to gain more light energy for the plasmonic photothermal effect. The results presented above indicate that $Cu_{2-x}Se$ HNSs are capable of rapidly generating localized heat under irradiation with a 1064 nm laser. This property makes them promising candidates for heat-involved therapeutic applications.

Enzymatic catalytic performance and mechanism

To investigate the combined catalytic therapeutic effect, the enzymatic catalysis activity and mechanism of $Cu_{2-x}Se$ HNSs in vitro were characterized (Fig. 4). The enzymatic catalytic mechanism is shown in Fig. 4a. The $Cu_{2-x}Se$ HNSs possess both POD- and CAT-like activities, which could catalyze H_2O_2 to ·OH for enzymatic therapy and catalyze H_2O_2 to O_2 as raw material for thermoelectric therapy, respectively. In addition, the photothermal effect of the $Cu_{2-x}Se$ HNSs can enhance both enzymatic activities. To gain more insights into the POD-like activity of $Cu_{2-x}Se$ HNSs, steady-state catalytic kinetics were determined in a PBS (pH 5.5) using 3,3',5,5'-tetramethylbenzidine (TMB) and H_2O_2 as substrates. Figure 4b shows the
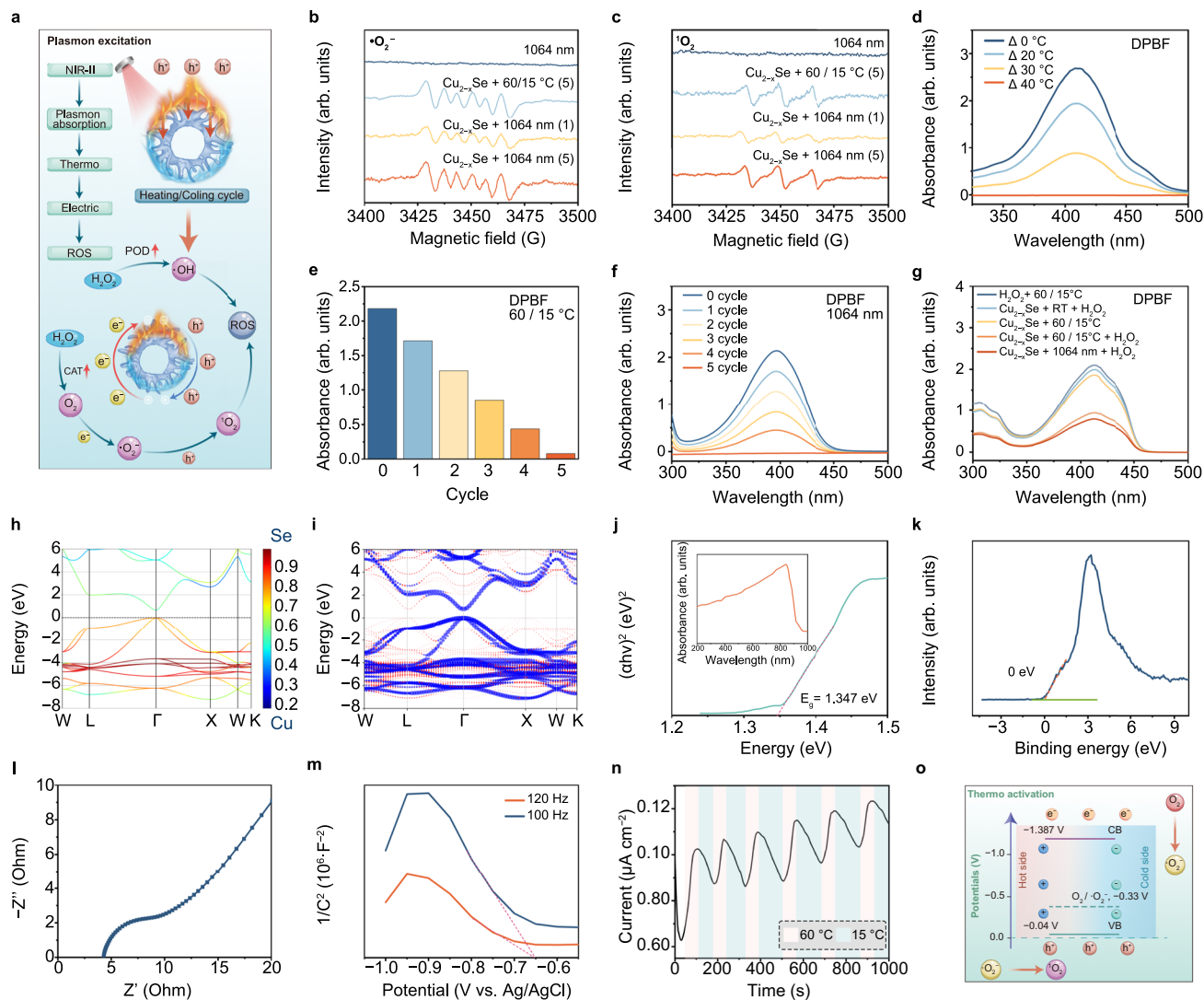
Fig. 5 | Exploration of the thermoelectric catalytic activities and mechanism.
a Schematic representation of the synergistic enzymatic and thermoelectric catalysis mechanism. **b**, **c** ESR spectra of $\cdot O_2^-$ trapped by DMPO (**b**) and $^1O_2$ trapped by TEMP (**c**) in $Cu_{2-x}Se$ HNSs and H_2O_2 mixed solution. **d**–**g** UV-vis absorption spectra of DPBF in $Cu_{2-x}Se$ HNSs and H_2O_2 solution versus temperature differences (**d**), heating cycles (**e**), laser radiation cycles (**f**), and H_2O_2 concentration (**g**) (Each cycle was heated and irradiated at 1064 nm (1.0 W cm^{-2}) for 5 min). **h**, **i** Band structures of Cu$_2$Se (**h**) and $Cu_{2-x}Se$ (**i**). Small red circles in (**i**) represent the defective states originating from the Cu vacancy. **j**, **k** Energy bandgap (**j**) and XPS valence band spectra (**k**) of $Cu_{2-x}Se$ HNSs. Insert in (**j**): UV-vis diffuse reflectance spectrum. **l** Electrochemical impedance spectroscopy under continuous heating. **m** Mott-Schottky plots. **n** Thermoelectric current under temperature variations. **o** Band structure diagram of $Cu_{2-x}Se$ HNSs. Source data are provided as a Source Data file (arb. units, arbitrary units).

changes in the absorbance of oxidated TMB (oxTMB) at 652 nm over time. The initial rate of $\cdot OH$ production (v_O) was determined by Beer-Lambert's law. The reaction rate was linear with the corresponding H_2O_2 concentration, and the Michaelis-Menten curve (Eq. 1) was fitted (Fig. 4c). [S] represents the concentration of the substrate. Subsequently, the maximum velocity (V_{max}) and Michaelis-Menten constant (K_m) were obtained using a Lineweaver-Burk plot (Eq. 2, Fig. 4d). V_{max} and K_m were determined to be 2.57×10^{-8} M s^{-1} and 30.01 mM, respectively, for $Cu_{2-x}Se$ HNSs at room temperature (RT) at about 21 °C. The low K_m and high V_{max} values indicate that $Cu_{2-x}Se$ HNSs exhibit a strong affinity for H_2O_2, providing efficient enzymatic reactions.

$$v_0 = \frac{V_{max} \cdot [S]}{K_m + [S]} \quad (1)$$

$$\frac{1}{v_0} = \frac{K_m}{V_{max}} \cdot \frac{1}{[S]} + \frac{1}{V_{max}} \quad (2)$$

Electron spin resonance (ESR) spectroscopy was employed to investigate the generation of $\cdot OH$ radicals, drawing inspiration from enzymatic activity. In this experimental setup, 5-diethyl-1-pyrroline-N-oxide (DMPO) was utilized as a trapping agent (as depicted in Fig. 4e). DMPO was chosen due to its ability to specifically interact with the transient $\cdot OH$ radicals, which have a short lifespan. In the ESR spectrum of $Cu_{2-x}Se$ HNSs at RT, the formed DMPO-OH compound exhibits a characteristic 1:2:2:1 signal, which is reliable evidence indicating the production of $\cdot OH$. To determine the influence of temperature, both a 60 °C water bath and 1064 nm irradiation for 5 min were used to heat

the Cu$_{2-x}$Se HNSs solution. The signal intensities exhibited a significant increase when the Cu$_{2-x}$Se HNSs solution underwent hot water bath treatment or laser irradiation, as compared to the signal at RT. This enhancement in signal intensity can be attributed to the heightened enzymatic activity under these conditions.

The oxTMB, formed through the oxidation of TMB by ·OH, exhibits a distinctive absorption peak at 652 nm. Consequently, TMB was selected as the chromogenic agent for the investigation of ·OH production. As shown in Fig. 4f, the enhanced absorbance of oxTMB with time indicates a positive correlation between the reaction time and ·OH generation. It is worth noting that the absorbance of oxTMB in Cu$_{2-x}$Se HNSs solution (80 μg mL^{-1}) increased with temperature (Fig. 4g), which is consistent with the ESR result. Besides, the 1064 nm laser treatment group achieved a TMB oxidation effect similar to that of the 60 °C water bath. These results suggest that Cu$_{2-x}$Se HNSs with higher temperatures exhibit much better POD-like activity, and can be switched to produce large amounts of ·OH by a 1064 nm laser for enhanced enzymatic therapy and photothermal therapy. The results suggest that the reaction temperature greatly affects the POD-like activity of Cu$_{2-x}$Se HNSs. Moreover, to compare the thermoelectric catalytic performance of spherical Cu$_{2-x}$Se (Cu$_{2-x}$Se (sp)) and Cu$_{2-x}$Se HNSs, we evaluated the efficiency of oxidized TMB under the same conditions. The TEM image of Cu$_{2-x}$Se (sp) is shown in Supplementary Fig. 1b. As shown in Supplementary Fig. 4b, the efficiency of oxidized TMB by Cu$_{2-x}$Se HNSs under the same conditions of heating/cooling and light exposure was significantly stronger than that of Cu$_{2-x}$Se (sp). It was demonstrated that Cu$_{2-x}$Se HNSs possessed a better thermoelectric catalytic performance.

We also found that Cu$_{2-x}$Se HNSs possess CAT-like activity which can catalyze H$_2$O$_2$ into O$_2$, and the activity can also be enhanced by the photothermal effect induced by 1064 nm radiation. To examine the O$_2$ production capacity, a dissolved oxygen meter was used for quantitative assessment (Fig. 4h). Effective O$_2$ production in the presence of H$_2$O$_2$ in Cu$_{2-x}$Se HNSs solution indicates excellent CAT-like activity. Moreover, following irradiation by a 1064 nm laser, the O$_2$ production rate was substantially increased. Therefore, the CAT-like activity was significantly improved; for instance, 27.6 mg L^{-1} of O$_2$ was generated after 20 min. It is important to note that the significant increase in O$_2$ production not only alleviates hypoxia in the tumor microenvironment but also has the potential to participate in other chain-catalyzed reactions requiring the participation of oxygen, for example, the thermoelectric catalytic process triggered by temperature fluctuations studied below.

V$_{Cu}$ not only promoted the plasmonic photothermal performance but also contributed to enzymatic activity. To explore the impact of V$_{Cu}$ on POD- and CAT-like activities, first-principles DFT calculations were performed using the Vienna ab initio simulation package (VASP). Figure 4i displays the optimized structures of defect-free Cu$_2$Se and defect-rich Cu$_{2-x}$Se. Figure 4j, k shows the proposed reaction mechanism for the POD-like pathway. The results suggest that the adsorption of H$_2$O$_2$ on the Cu$_2$Se surface is exothermic (− 0.48 eV), and its dissociation into 2OH* further leads to an energy release of 2.76 eV. However, in the presence of V$_{Cu}$, both the adsorptions of H$_2$O$_2$* and 2OH* on the Cu$_{2-x}$Se surface are more energetically favorable, indicating that V$_{Cu}$ facilitates the formation of OH species and is, therefore, favorable for the POD-like activity. In addition, the critical intermediates adsorbed on different surfaces can also have a significant impact on the CAT-like activity, as illustrated in Fig. 4l, m. To produce active O$_2$, the thermodynamic energy barriers of the dehydrogenation of OH* to form O* and then O$_2$* on the Cu$_2$Se surface are 1.17 and 0.40 eV per oxygen, respectively, which are very close to the values on the Cu$_{2-x}$Se surface. This endothermic process was confirmed by the experimental results in Fig. 4e−g. Furthermore, as the desorption of O$_2$* to form active O$_2$ on the Cu$_{2-x}$Se surface is slightly favorable, Cu$_{2-x}$Se HNSs thus show higher CAT-like activity with applied thermal

energy. Therefore, the photo-thermoelectric effect, which provides thermal energy, is helpful for endothermic processes.

Plasmonic photo-thermoelectric catalytic performance and mechanism

To elucidate the comprehensive plasmonic photothermal performance and thermoelectrically coupled enzymatic catalysis activities of Cu$_{2-x}$Se HNSs in vitro, a characterization was conducted. Figure 5a shows a schematic of the plasmonic photo-thermoelectric catalytic mechanisms of Cu$_{2-x}$Se HNSs based on plasmonic heat and the Seebeck effect[16]. After the absorption of 1064 nm photons on one side of the Cu$_{2-x}$Se HNSs, plasmonic heat, and temperature difference serve as the driving force to directionally move the electrons and holes based on the Seebeck effect. Cu$_{2-x}$Se is a conventional p-type semiconductor known for the propensity to supply holes that facilitate carrier diffusion in the heating/cooling cycle, resulting in the generation of a built-in electric field. This generated electric field serves to enhance the separation and conveyance of e$^-$-h$^+$ pairs, subsequently guiding them to the surface of Cu$_{2-x}$Se HNSs for further participation in the catalytic reaction. Ultimately, the electrons in the conduction band (CB) effectively catalyze the formation of ·O$_2^-$ from O$_2$, while the holes in the VB can react with ·O$_2^-$ to produce ^{1}O$_2$.

The pathway involving the processes of NIR-II → plasmonic absorption → thermo → electric → ROS was verified via ESR and UV-vis spectrophotometer utilizing 1,3-diphenylisobenzofuran (DPBF) indicator. Various test groups were established, including the 1064 nm irradiation group and the RT group as controls, irradiation/natural cooling cycle groups, and heating/cooling cycle groups. To confirm ROS generation, ESR spectroscopy was employed (Fig. 5b, c), employing DMPO and 2,2,6,6-tetramethylpiperidine (TEMP) dissolved in methanol as spin trapping agents for ·O$_2^-$ and ^{1}O$_2$, respectively. In both figures, no signal peaks were observed for water irradiated by the 1064 nm laser, indicating the absence of ROS generation. Subsequently, the Cu$_{2-x}$Se HNSs solution was subjected to a cycle of heating to 60 °C in a water bath, followed by cooling to 15 °C in an ice bath. After five excitation cycles, characteristic sextuplet peaks corresponding to ·O$_2^-$ and three peaks matching the ^{1}O$_2$ were observed. This observation indicated that Cu$_{2-x}$Se HNSs can produce ·O$_2^-$ and ^{1}O$_2$ catalyzed by separated e$^-$ and h$^+$ through the thermoelectric effect. Notably, ·O$_2^-$ plays a crucial role in the oxidative chain reaction induced by free radicals, which can trigger the production of ^{1}O$_2$ via its mutation or reaction with h$^+$. Therefore, the presence of a ^{1}O$_2$ characteristic peak aligns perfectly with the generation of ·O$_2^-$ and further confirms that the generation of ^{1}O$_2$ by Cu$_{2-x}$Se HNSs occurs through the chain reaction based on ·O$_2^-$. Similarly, when the Cu$_{2-x}$Se HNSs solution was heated by a 1064 nm laser for 5 min, both signal peaks of ·O$_2^-$ and ^{1}O$_2$ were observed. More notably, after five irradiation/natural cooling cycles, both observed signals were significantly amplified. This behavior is attributed to the enduring plasmonic photothermal capabilities of Cu$_{2-x}$Se HNSs, which maintain the ability to facilitate the separation of e$^-$ and h$^+$ for cascade catalytic reactions: O$_2$ + e$^-$ → ·O$_2^{2-}$ and ·O$_2^-$ + h$^+$ → ^{1}O$_2$. Accordingly, the proposed principle of plasmonic photothermal effect, thermoelectricity, and catalytic reaction was conclusively validated.

To further verify ROS generation, a DPBF indicator with absorption at 410 nm was employed as it can be decomposed into 1,2-dibenzoylbenzene via reaction with ·O$_2^-$ and ^{1}O$_2$. Normally, this property is used to reveal ·O$_2^-$ and ^{1}O$_2$ generation through UV-visible absorption spectroscopy. To this end, experiments were first conducted at various temperature differences (Fig. 5d). When the temperature differences were increased, the absorbance of DPBF in Cu$_{2-x}$Se HNSs solution decreased, as larger temperature differences endowed more effective e$^-$-h$^+$ pair separation and higher thermoelectric efficiency. Therefore, the maximum possible temperature difference was employed for subsequent experiments, typically setting

the high temperature to about 60 °C, when taking biological tolerance into consideration. The impact of heating/cooling and irradiation/natural cooling excitation cycles on DPBF absorbance is clarified in Fig. 5e, f. When the number of excitation cycles is increased, the $\cdot O_2^-$ and $^1O_2$ generation ability also increases. It is worth noting that the changed absorbance value is consistent for each additional cycle, demonstrating the stable pathway of plasmonic photothermal effect, thermoelectricity, and catalytic reaction in $Cu_{2-x}Se$ HNSs. In other words, if irradiation is cyclically turned on and off, the temperature increases and decreases accordingly, and ROS can be generated continuously and stably.

We also investigated the influence of the H_2O_2 concentration on ROS production to clarify the potential of the cascade reactions in therapy (Fig. 5g). The UV-vis absorption peaks of DPBF in H_2O_2 solution under heating/cooling excitation, or $Cu_{2-x}Se$ HNSs and H_2O_2 mixed solution at RT show slight differences due to the scarcely produced $\cdot O_2^-$ and $^1O_2$. In contrast, the absorbance of DPBF in the $Cu_{2-x}Se$ HNSs solution under heating/cooling (or 1064 nm irradiation) excitation is decreased, because the oxygen in water can be transferred to $\cdot O_2^-$ and $^1O_2$ in sequence *via* a thermoelectric mechanism. Notably, the absorbance of DPBF in H_2O_2 and $Cu_{2-x}Se$ HNSs mixed solution under heating/cooling excitation greatly decreased due to the generation of large amounts of $\cdot O_2^-$ and $^1O_2$, which can be attributed to the increased O_2 from H_2O_2 as a result of the CAT-like activity of $Cu_{2-x}Se$ HNSs. Moreover, the CAT-like performance can be significantly enhanced by increasing the temperature, which may generate more oxygen for transfer to ROS. Then, the photothermal effect of $Cu_{2-x}Se$ HNSs separates free e^- and h^+, which subsequently combine with the generated oxygen to promote the production of $\cdot O_2^-$ and $^1O_2$. Accordingly, two cascade reactions occur, including plasmonic photothermal triggered and enhanced reactions of $H_2O_2 \rightarrow O_2 \rightarrow \cdot O_2^- \rightarrow {}^1O_2$ and $H_2O_2 \rightarrow \cdot OH$, which show huge application prospects in anti-cancer catalytic therapy due to efficient ROS generation from excessive H_2O_2 in cancer cells[53–55].

As an ideal narrow-band semiconductor, stoichiometric Cu_2Se has high carrier mobility and low resistivity. However, the narrow band of Cu_2Se leads to a great increase in the probability of the recombination of separated e^- and h^+. In addition, the carriers reach the bottom of the CB by nonradiative relaxation, and a part of the energy greater than the band gap is converted into lattice vibrational heat, which is not conducive to the full utilization of energy. This also indicates that the redox potential is not high, which is not conducive to improving the catalytic reaction. Therefore, we constructed $Cu_{2-x}Se$ HNSs with a reasonably narrow bandgap by introducing V_{Cu} through defect engineering.

To reveal the role of V_{Cu}, the energy band structures and thermoelectric properties of Cu_2Se and $Cu_{2-x}Se$ were investigated *via* DFT calculations. The computational results shown in Fig. 5h indicate that Cu_2Se is a direct-bandgap semiconductor with a bandgap of 0.657 eV, which is lower than the experimental value because of the well-known DFT problem[56]. The VB is primarily composed of the contributions from Se atoms (red), whereas the CB is dominated by Cu (blue), which is consistent with previous reports[56]. With the introduction of V_{Cu}, the energy band structure of $Cu_{2-x}Se$ (Fig. 5i) undergoes significant changes, and its bandgap increases to 0.787 eV owing to the Moss-Burstein effect. More importantly, it is confirmed that the triplet and singlet degenerate energy levels appear at the VB maximum and CB minimum, respectively, at the L point of the Brillouin zone. This notably increases the density of states near the Fermi level, being responsible for the improvement in the electrical conductivity of $Cu_{2-x}Se$.

The UV-vis diffuse reflectance spectrum, as depicted in Fig. 5j, provides the data needed to calculate the bandgap (E_g) of the $Cu_{2-x}Se$ HNSs, which is determined to be 1.347 eV using the Tauc plot. As depicted in Fig. 5k, the Fermi energy level (E_f) of $Cu_{2-x}Se$ HNSs penetrates the VB, and the difference between the E_f and the VB is 0 eV. This

observation indicates that $Cu_{2-x}Se$ HNSs exhibit characteristics of a *p*-type semiconductor with excellent conductivity. Figure 5l shows the results of electrochemical impedance spectroscopy conducted on $Cu_{2-x}Se$ HNSs to assess the transfer rate of e^- and h^+. The small arc diameter observed for $Cu_{2-x}Se$ HNSs endows a low charge transfer resistance, namely, a high electron transfer rate. This outcome can be attributed to the formation of a built-in electric field within $Cu_{2-x}Se$ HNSs through the thermoelectric effect, enabling the continuous escape of holes, while the presence of V_{Cu} on the surface may impede the recombination of e^- and h^+. From Fig. 5m, the flat band potential *vs* Ag/AgCl electrode (E_{fb} *vs* Ag/AgCl) of the $Cu_{2-x}Se$ HNSs can be determined to be -0.65 V. Thus, E_{fb} versus the normal hydrogen electrode (NHE) was calculated using Eq. 3:

$$E_{fb} \, (vs \, NHE) = E_{fb} \, (vs \, Ag/AgCl) + E_{Ag/AgCl} + 0.059 \times pH \qquad (3)$$

where the pH of the Na_2SO_4 electrolyte is 7, and $E_{Ag/AgCl}$ is 0.197 V at 25 °C. The value of E_{fb} (*vs* NHE) was calculated to be -0.04 V. In the XPS valence band spectrum, the difference between the Fermi energy level and the VB was 0. Therefore, the VB of $Cu_{2-x}Se$ HNSs was determined to be -0.04 V. The negative slope of the Mott–Schottky curve corresponded to the *p*-type semiconductor of $Cu_{2-x}Se$ HNSs. Figure 5n provides the current test results of the $Cu_{2-x}Se$ HNSs under six heating/cooling excitation cycles. A stable response of the photo-thermoelectric current with time was observed in six repeated cycles for the $Cu_{2-x}Se$ HNSs. The high current signals with stability implied that $Cu_{2-x}Se$ HNSs promote carrier separation and migration under temperature fluctuations. The band structure diagram of $Cu_{2-x}Se$ HNSs was obtained based on the abovementioned results (Fig. 5o). The potential of CB was calculated to be -1.387 V, which is significantly more negative than the redox potential of $O_2/\cdot O_2^-$; this indicates that the electrons in the CB possess the necessary energy levels to facilitate the favorable redox reaction of O_2 to $\cdot O_2^-$. In addition, the temperature difference triggers the movement of h^+ in the heating/cooling cycle of $Cu_{2-x}Se$ HNSs, resulting in the separation of e^- and h^+ for the thermoelectric catalytic effect. At the same time, the separated electrons participate in the catalytic conversion of O_2 to $\cdot O_2^-$, and the holes on the VB react with $\cdot O_2^-$ to form $^1O_2$, further facilitating the catalytic reaction process.

Thermoelectric materials can directly convert thermal energy into electrical energy. The thermoelectric performance can be characterized by the dimensionless figure of merit (ZT), $ZT = S^2 \cdot \sigma \cdot T/\kappa$, which is determined by the physical parameters of the Seebeck coefficient (S), electrical conductivity (σ), thermal conductivity (κ), and absolute temperature (T). The power factor is represented by $S^2\sigma$, whereas the Seebeck coefficient measures the thermoelectric voltage generated by a temperature difference ($S = dV/dT$) in the material. Typically, there are several approaches to boosting the ZT value, including doping, engineering band structures, decoupling thermoelectric parameters, and the development of materials[1,57,58]. $Cu_{2-x}Se$ is a self-doping material with abundant V_{Cu}, which is conducive to regulating thermoelectric performance. The thermoelectric performance of $Cu_{2-x}Se$ HNSs after spark plasma sintering was summarized in Supplementary Figs. 5 and 6. It should be noted that the κ of $Cu_{2-x}Se$ HNSs exhibits a gradual increase with temperature while remaining below $0.50 \, W \, m^{-1} K^{-1}$, which is low for thermoelectric materials, particularly in the low-temperature range. The ZT value ranged from 0.011 to 0.015 at a low sintering temperature of 673 K, demonstrating the thermoelectric property of $Cu_{2-x}Se$ HNSs.

Synergetic mechanism of thermoelectric effect

To further reveal the impact of V_{Cu}, Fig. 6 shows the microscopic origin of the change of the electronic structures and the thermoelectric properties of Cu_2Se and $Cu_{2-x}Se$. Figure 6a, b illustrates the partial density of states (PDOS) of Cu_2Se and $Cu_{2-x}Se$. Compared with Cu_2Se,
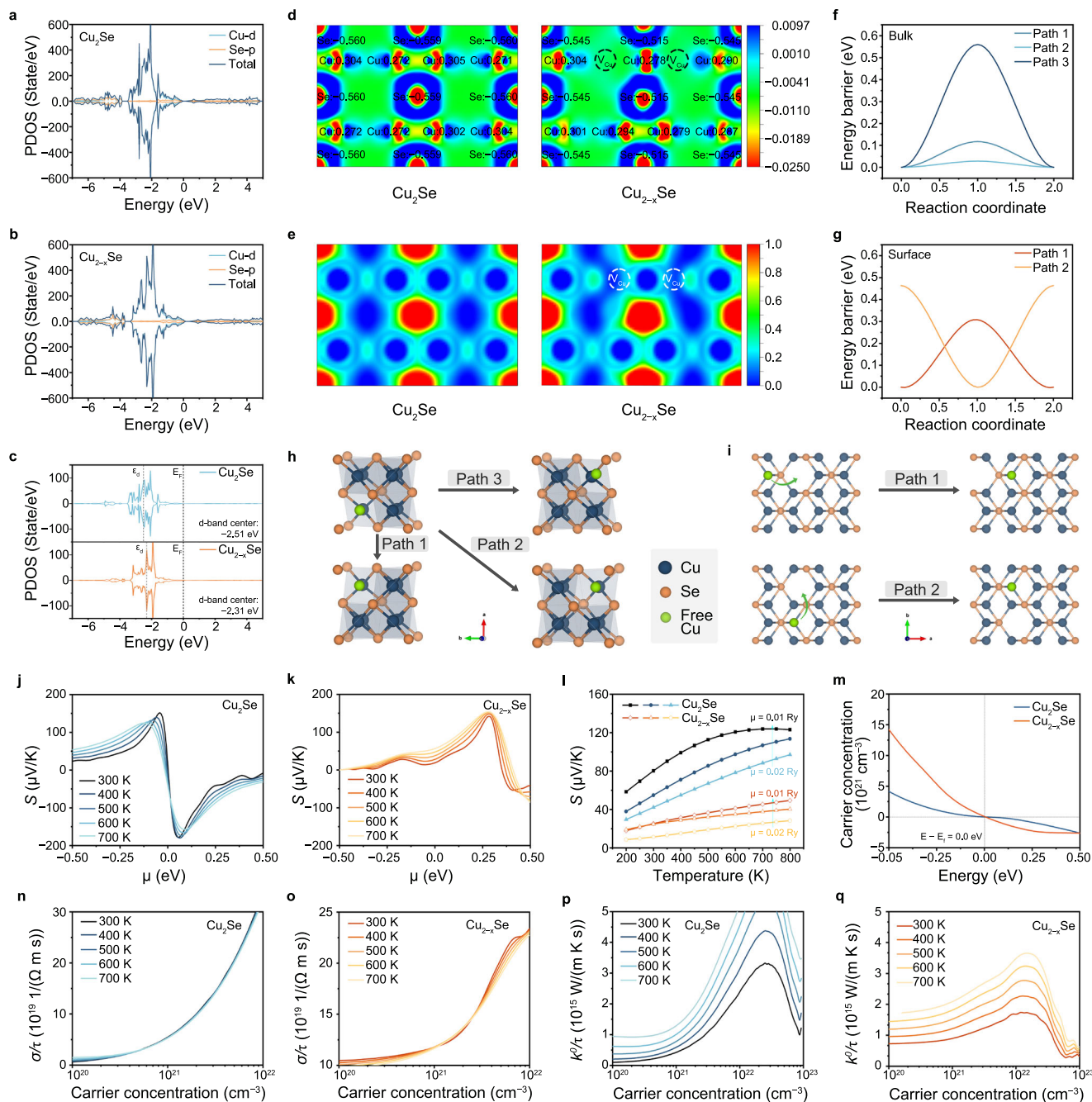
Fig. 6 | Thermoelectric properties of Cu₂Se and Cu₂₋ₓSe. **a–e** The PDOS profiles (**a**, **b**), PDOS of Cu 3d states (**c**), electron density difference images (**d**), and electron localization function for Cu₂Se and Cu₂₋ₓSe surfaces (**e**). **f**, **g** Diffusion barriers of Cu ions in different paths for Cu₂₋ₓSe bulk and surface. **h**, **i** Possible diffusion schemes of Cu ions in bulk and surface of Cu₂₋ₓSe. **j–q** Seebeck coefficient (**j–l**), carrier concentration (**m**), electrical conductivity (**n**, **o**), and electronic part of the thermal conductivities (**p**, **q**) for Cu₂Se and Cu₂₋ₓSe. Source data are provided as a Source Data file.

the Cu-3d band of Cu₂₋ₓSe shifts toward higher energy positions, accompanied by an increase in the band gap (Fig. 5h, i, 6c). As a result, either the generated electrons possess higher reduction activity, or the generated holes show higher oxidation activity. As a result, Cu₂₋ₓSe will have a superior redox capability. In addition, Fig. 6c shows that the introduction of V_Cu in Cu₂Se upshifts the d-band center of Cu from − 2.51 eV to − 2.31 eV. The d-band center was much closer to the Fermi level, and fewer electrons occupied the antibonding states formed between Cu and the adsorbed intermediates, demonstrating a stronger adsorbate-metal interaction[59]. This explains why Cu₂₋ₓSe exhibits superior POD-like and CAT-like activities during catalytic reactions. Based on the electron density difference shown in Fig. 6d, an evident

charge redistribution around the Cu ions adjacent to V_Cu was confirmed. In addition, the Bader charge values of all Cu metals that can serve as active sites were averaged. It is found that the average Bader charge of all surface Cu sites in Cu₂Se is 0.282, while that in Cu₂₋ₓSe is 0.309. Therefore, the valence state is increased by the formation of V_Cu, which is consistent with the shift in the d-band center, as shown in Fig. 6c. Meanwhile, the bonding of these Cu ions with the surrounding ions weakened, as indicated by the electron localization function (Fig. 6e). After the formation of defects, charge redistribution and the higher oxidation state of the active sites will facilitate the oxidation of H₂O₂ to form O₂, being favorable for the much more improved catalytic activity of the material.

To investigate the diffusion dynamics of Cu ions, we simulated diffusion pathways and calculated the corresponding energy barriers using the nudged elastic band method. Initially, we explored three potential migration pathways and their associated diffusion barriers for Cu ions within the bulk phase (as shown in Fig. 6f, h). In this context, the highly symmetric cubic phase structure of $Cu_{2-x}Se$ at RT offers Cu ions structurally equivalent sites. Based on the diffusion barrier diagram, we found that the energy barriers for paths 1, 2, and 3 are 0.1170, 0.0280, and 0.5602 eV, respectively. Notably, the energy barrier for path 2 was the lowest among them. These findings indicate that Cu ions can readily diffuse within the bulk phase. Subsequently, we compared Cu ion migration on the surface, specifically examining paths 1 and 2 (as illustrated in Fig. 6g, i). It is noteworthy that the diffusion energy barriers for paths 1 and 2 remained low, which facilitates ion migration. Consequently, the high mobility of Cu ions may induce substantial phonon scattering and inhibit the propagation of transverse waves to disrupt the heat propagation by phonons, which is confirmed to significantly decrease the thermal conductivity and thus enhance the electrothermal performance of Cu_2Se[60].

The Seebeck coefficient, carrier concentration, electrical conductivity, and thermal conductivities of Cu_2Se and $Cu_{2-x}Se$ were computed using the BoltzTrap code[61]. The presence of V_{Cu} within the crystal led to changes in the band structure, which in turn affected the thermoelectric properties of $Cu_{2-x}Se$. Figure 6j, k illustrates the relationship between the Seebeck coefficient and the chemical potential. For Cu_2Se, it can be identified clearly that the *p*-type Seebeck coefficients near Fermi energy ($E - E_f = 0.0$ eV, $[-0.05$ eV, -0.03 eV]) ranged from 35.52 to 151.62 μV/K, which are much higher than those for $Cu_{2-x}Se$ (Fig. 6l). To clarify the phenomenon, the carrier concentration as a function of chemical potential is also calculated. The data in Fig. 6m confirm that the presence of V_{Cu} leads to an obvious increase of the carrier concentration, and the values for $Cu_{2-x}Se$ are 4-6 folds higher than those for Cu_2Se, well in agreement with previous experimental observations[60,62]. Although the increased carrier concentration in $Cu_{2-x}Se$ is unfavorable for the Seebeck coefficient, it is very beneficial for the enhancement of the electric conductivity. As illustrated in Fig. 6n, o and Supplementary Fig. 7a–c, even at the same carrier concentration, the electrical conductivity of $Cu_{2-x}Se$ remains much higher than that of Cu_2Se, and the increment in carrier concentration further exacerbates such an advantage. This phenomenon may be related to the defect states and multi-energy-valley characteristics at the L point of the Brillouin Zone of $Cu_{2-x}Se$ (Fig. 5i). With increasing temperature, the electric conductivity of $Cu_{2-x}Se$ shows a slight decrease at a certain point (Supplementary Fig. 7c), in line with our experimental observations in Supplementary Fig. 5. Furthermore, the results in Fig. 6p, q and Supplementary Fig. 7d–f demonstrate that the electric part of the thermal conductivity for the *p*-type carriers exhibits a noticeable increase with increasing temperature for both Cu_2Se and $Cu_{2-x}Se$, also being consistent with experimental tests (Supplementary Fig. 6). When Cu_2Se deviates from the stoichiometry, the thermal conductivity of $Cu_{2-x}Se$ is higher than that of Cu_2Se, yet it can still retain at a low value, which is originated from the much higher phonon scattering of $Cu_{2-x}Se$ and the liquid-like super-ionic behavior as discussed above[60]. Although it is expected that the *ZT* value of $Cu_{2-x}Se$ is lower than that of Cu_2Se, it still exhibits good thermoelectric performance. More importantly, the obvious increment of the hole concentration is very helpful for the catalytic oxidation process, while the higher oxidation state of the active site is crucial for the adsorption and reaction of H_2O_2. These factors together synergistically improve the overall photothermal performance of the material.

In vitro therapeutic effect

The preceding characterization results have confirmed the photothermal conversion and ROS generation capabilities of $Cu_{2-x}Se$ HNSs when exposed to 1064 nm excitation. Building upon these findings, the therapeutic effects and mechanisms of these materials at the cellular level were investigated. A schematic diagram illustrating the induction of cell cuproptosis and apoptosis through the action of copper ions, ROS, and heat is depicted in Fig. 7a. Prior to delving into the treatment mechanism and efficacy, the cytotoxicity of $Cu_{2-x}Se$ HNSs toward L929 fibroblast cells and CT26 colon cancer cells was assessed using the standard methylthiazolium tetrazolium (MTT) assay. In Supplementary Fig. 8a, the survival rate of L929 cells co-incubated with different concentrations of $Cu_{2-x}Se$ HNSs after 12 and 24 h was high, even with a high concentration of 100 μg mL^{-1}, demonstrating the good biosafety and biocompatibility of $Cu_{2-x}Se$ HNSs for cells. The in vitro cytotoxicity was determined using CT26 colon cancer cells subjected to various treatments (Fig. 7b). Compared with the control group, 1064 nm laser irradiation showed negligible inhibition of cell viability, indicating the safety of the excitation source. However, cells cultivated with $Cu_{2-x}Se$ HNSs exhibited a noticeable increase in cell death rate, attributed to the therapeutic effect of ·OH generated from the POD-like activity. Importantly, the viabilities of cells treated with $Cu_{2-x}Se$ HNSs under 1064 nm laser irradiation declined sharply. Furthermore, the cellular activity decreased in a $Cu_{2-x}Se$ HNSs concentration-dependent manner, highlighting the achievement of efficient cytotoxicity. The cells were ultimately killed by the combined effects of photothermal, thermally-enhanced enzymatic, and thermoelectric catalytic activities of $Cu_{2-x}Se$ HNSs, which collectively generated heat and large amounts of ROS for effective cell elimination. To demonstrate the importance of $Cu_{2-x}Se$ sample morphology for thermoelectric catalysis, we examined the cell-killing effect of $Cu_{2-x}Se$ (sp) using the MTT method under the same conditions (Supplementary Fig. 8b). Although high concentrations of $Cu_{2-x}Se$ (sp) also showed a cell-killing effect, it is clear that they are less effective than $Cu_{2-x}Se$ HNSs. This highlights the significance of morphology in thermoelectric catalytic treatment.

Subsequently, the ROS-generating ability of $Cu_{2-x}Se$ HNSs in CT26 cells was investigated utilizing 2',7'-dichlorofluorescein diacetate (DCFH-DA) as an ROS probe. When DCFH-DA enters the cell through the cell membrane, it is oxidized by ROS to produce the green fluorescent 2',7'-dichlorofluorescein (DCF). The fluorescence intensity of DCF indicated the amount of intracellular ROS. In Fig. 7c and Supplementary Fig. 9a, confocal laser scanning microscopy (CLSM) images of cells treated with the control group or 1064 nm group show almost no green fluorescence owing to the lack of ROS production. Conversely, the cells treated with $Cu_{2-x}Se$ HNSs and 1064 nm laser emitted significantly enhanced fluorescence, even much stronger than that of cells treated with non-excited $Cu_{2-x}Se$ HNSs; the phenomenon can be attributed to the limited ROS generated within the cells through the enzymatic catalysis of $Cu_{2-x}Se$ HNSs alone. However, when the 1064 nm laser was introduced, there was a substantial increase in ROS production due to both thermal-enhanced enzymatic and thermoelectric catalysis. To further distinguish the cell-killing contribution of different kinds of ROS, we detected and quantified intracellular ·OH, $^1O_2$, and ·O_2^- using specific ROS probes of aminophenyl fluorescein (APF), singlet oxygen sensor green (SOSG), and dihydroethidium (DHE), respectively. As demonstrated in Supplementary Fig. 9b–d, the levels of ·OH, $^1O_2$, and ·O_2^- produced were consistent with the overall trend of total ROS levels indicated by DCFH-DA, as supported by the quantitative fluorescence analyses in Supplementary Fig. 9e–h. These results align with those obtained from ESR and color reactions in solution. The accumulation of significant ROS levels within the cells is expected to induce cuproptosis and apoptosis, as evidenced by western blotting and cell staining.

Cuproptosis, a process characterized by the aggregation of lipoylated proteins and the loss of Fe-S cluster proteins in the mitochondria induced by the accumulation of copper in cells, represents a regulator of cell death[38]. To reveal whether cuproptosis occurred during the therapeutic process, the hallmarks of dihydrolipoamide
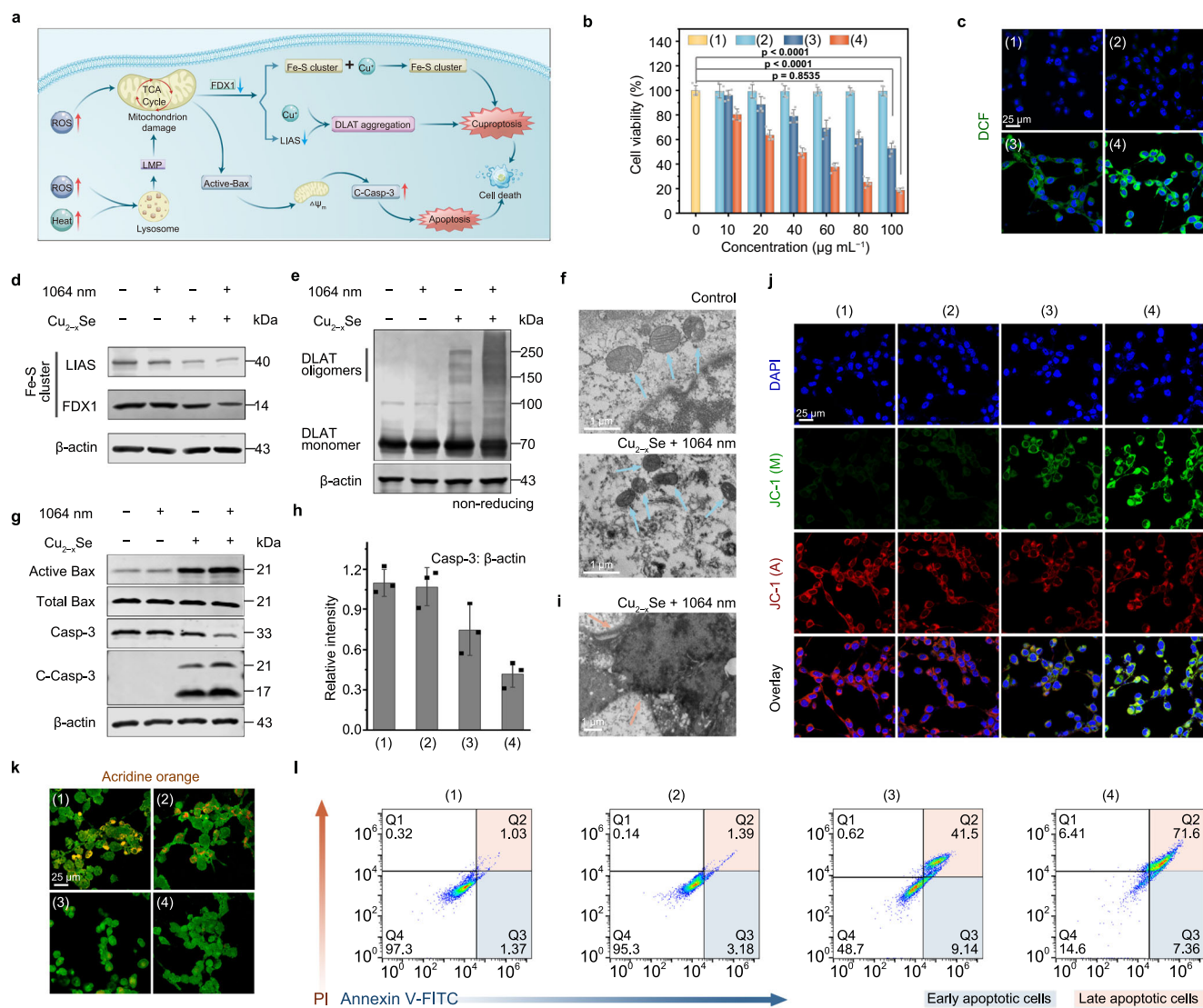
Fig. 7 | In vitro evaluation of anti-tumor properties. a Schematic diagram of the cuproptosis and apoptosis caused by Cu ions, ROS, and heat. **b** Cytotoxicity of CT26 cells treated with (1) Control, (2) 1064 nm, (3) Cu$_{2-x}$Se HNSs, (4) Cu$_{2-x}$Se HNSs + 1064 nm. Data presented as mean ± S.D. (n = 5 biologically independent cell samples). **c** CLSM images of CT26 cells stained with DAPI and DCFH-DA after different treatments. **d**, **e** Western blotting analysis on the expression levels of cuproptosis-related proteins (LIAS, FDX1, and DLAT) in CT26 cells treated with various conditions. **f** Bio-TEM images of mitochondria in CT26 cells before and after Cu$_{2-x}$Se HNSs + 1064 nm treatment. **g** The expression levels of apoptosis-related

proteins (active Bax, total Bax, Casp-3, and C-Casp-3) in CT26 cells treated with various conditions examined by western blotting. **h** Western blotting intensity ratio of Casp-3 and β-actin. Data presented as mean ± S.D. (n = 3 biologically independent cell samples). **i** Bio-TEM images of CT26 cells after Cu$_{2-x}$Se HNSs + 1064 nm treatment. **j–l** CLSM images of CT26 cells stained with DAPI and JC-1 (**j**), acridine orange (**k**), and flow cytometry analysis (**l**) of the apoptosis of CT26 cells after different treatments. The 1064 nm laser irradiation time: 5 min. Source data are provided as a Source Data file.

S-acetyltransferase (DLAT), Fe-S cluster proteins ferredoxin 1 (FDX1), and lipoyl synthase (LIAS) were detected by western blotting. It was found that Cu$_{2-x}$Se HNSs + 1064 nm treatment could destabilize FDX1 and LIAS significantly (Fig. 7d, e), promoting DLAT oligomerization to induce cuproptosis. Similar conclusions were obtained by immunohistochemistry of LIAS (Supplementary Fig. 10) In addition, the GSH in tumors can be consumed by massive Cu$^+$ from Cu$_{2-x}$Se HNSs (Supplementary Fig. 4a), further promoting cuproptosis. Taken together, FDX1 and LIAS are upstream regulators of protein lipidosis that promote the aggregation of mitochondrial proteins and the loss of Fe-S clusters. Excessive uptake of Cu by cells leads to the binding of Cu to DLAT in the tricarboxylic acid (TCA) cycle of mitochondria, inducing the aggregation of these proteins. These abnormal processes lead to protein toxicity stress and, ultimately, cell death, namely, cuproptosis. Moreover, the morphological changes of the mitochondria in CT26

cells treated with Cu$_{2-x}$Se HNSs were observed by bio-TEM. As depicted in Fig. 7f and Supplementary Fig. 11, arrows indicate the mitochondria. Obviously, Cu$_{2-x}$Se HNSs assisted with 1064 nm laser caused severe mitochondria damage, which was manifested as increased membrane density, reduced mitochondrial volume, reduced or even absence of mitochondria cristae, and even swelling and cavitation in mitochondria. To sum up, Cu$_{2-x}$Se HNSs could generate ROS, accumulate Cu ions, and induce mitochondrial damage, resulting in cuproptosis.

Considering that citrate and α-Ketoglutarate (α-KG) are important metabolites in TCA cycle[38,63], we separately measured their contents after treating the cells under various conditions. The relative content levels of citrate and α-KG were measured by a colorimetric reaction. As shown in Supplementary Fig. 12a, b, compared to the control group, the cells in the 1064 nm group showed no significant changes in the

contents of citrate and α-KG. In contrast, the Cu$_{2-x}$Se HNSs and Cu$_{2-x}$Se HNSs + 1064 nm groups exhibited an apparent increase in citrate and a significant decrease in α-KG. The effects were even more pronounced in the Cu$_{2-x}$Se HNSs + 1064 nm group. The result is consistent with the trend of formation of DLAT oligomers which is closely related to the occurrence of cuproptosis (Fig. 7e). Besides, given the importance of oxygen for the proper conduct of TCA cycle and its necessity in the occurrence of cuproptosis, we then detected the oxygen consumption rate after the cells were treated under various conditions (Supplementary Fig. 12c). Compared with the control group, the cells in 1064 nm group did not induce obvious changes both in basal respiration and spare respiration capacity (Supplementary Fig. 12d, e), while treatment with Cu$_{2-x}$Se HNSs or Cu$_{2-x}$Se HNSs + 1064 nm significantly reduces the basal respiration and spare respiration capacity. As expected, the Cu$_{2-x}$Se HNSs + 1064 nm group had a more substantial effect than other groups. The above results confirm that the plasmonic-thermoelectric catalytic therapy can effectively cause mitochondria dysfunction, including abnormalities in the TCA cycle.

To gain a deeper understanding of the mechanisms underlying cell death, we also investigated apoptosis, a normal genetically programmed cell death process. Mitochondria play a crucial role in regulating apoptosis. Within mitochondria, the Bax family interacts with the Bcl-2 family, leading to changes in the permeability of the mitochondrial membrane, resulting in the loss of transmembrane potential and the release of proteins that trigger cascade reactions involving the caspase (Casp) pathway. Based on the representative Western blots of the pro-apoptotic protein Bax, it was observed that active Bax expression in mitochondria significantly increased following treatment with Cu$_{2-x}$Se HNSs + 1064 nm, and noticed changes were observed in the Cu$_{2-x}$Se HNSs treated group (Fig. 7g, h). Consequently, cleaved Casp-3 (C-Casp-3) was activated to initiate apoptosis. The Cu$_{2-x}$Se HNSs group, which produced fewer ROS, exhibited limited impact on active Bax and C-Casp-3 expression, whereas the Cu$_{2-x}$Se HNSs + 1064 nm group generated large amounts of ROS and heat, which significantly influenced the expression of active Bax and C-Casp-3. Furthermore, the morphological changes of the CT26 cells treated with Cu$_{2-x}$Se HNSs + 1064 nm were shown by bio-TEM in Fig. 7i. The reduced cell volume, condensation, and intranuclear chromatin condensation were observed, indicating the cell apoptosis.

Based on these results, we expect that active Bax can trigger mitochondrial membrane permeability because the change in mitochondrial membrane potential is a hallmark of early apoptosis, which can be detected by the J-aggregate-forming lipophilic cation 1 (JC-1) probe. The JC-1 probe can penetrate the undamaged mitochondrial membrane and form aggregates, abbreviated as JC-1 (A), which emit red fluorescence within the mitochondrial matrix. When the mitochondrial membrane potential is low, the probe cannot aggregate in the mitochondrial matrix and exists as a JC-1 monomer, abbreviated as JC-1 (M), to produce green fluorescence. Figure 7j shows CLSM images of cells subjected to different JC-1 staining treatments. The cells in the control and 1064 nm groups emitted intense red fluorescence, indicating that the cell membrane was not damaged and that the mitochondrial membrane potential was high. Notably, the cells treated with Cu$_{2-x}$Se HNSs showed weak green fluorescence of JC-1 (M), while the green-red fluorescence ratio increased significantly after the introduction of the 1064 nm laser. The results indicate that the treatment of Cu$_{2-x}$Se HNSs + 1064 nm causes severe damage to the mitochondrial membrane. After that, the change of mitochondrial membrane potential further activated C-Casp-3, as shown in Fig. 7g, where the activity of C-Casp-3 in Cu$_{2-x}$Se HNSs + 1064 nm treated cells was increased obviously. Accordingly, active Bax increased mitochondrial membrane permeability and further activated C-Casp-3 to initiate apoptosis.

Lysosomes are key organelles involved in apoptosis and can damage the internal structure of cells *via* lysosome-mitochondria crosstalk[64]. Hence, the permeabilization and integrity of the lysosomes were assessed with acridine orange as an indicator (Fig. 7k and Supplementary Fig. 13a). In normal cells, acridine orange can cross the cell membrane, stain the nucleus and cytoplasm, and emit green fluorescence while emitting red fluorescence in acidic lysosomes, similar to the CLSM images of cells in the control and 1064 nm groups. After the treatment of the Cu$_{2-x}$Se HNSs + 1064 nm group, the red fluorescence decreased sharply, indicating damage to the lysosomal structure and an increase in lysosomal membrane permeabilization. As a result, lysosomal proteases are released and act on the mitochondria, initiating mitochondrial destabilization and triggering downstream apoptotic cascades, such as caspase activation and apoptosis[65,66], as shown in Fig. 7a.

To determine the overall effect of these actions, we used Calcein-AM and propidium iodide (PI) to co-stain CT26 cells. Typically, cells emitting red fluorescence are dead, and cells emitting green fluorescence are alive. As expected, in Supplementary Fig. 13b, the CLMS images showed that the cells were alive in the control and 1064 nm treatment groups, as evidenced by strong green fluorescence. Conversely, the cells in the Cu$_{2-x}$Se HNSs group showed a decrease in green fluorescence and an increase in red fluorescence due to the therapeutic effect and death mechanism induced by enzymatic catalysis. More impressively, the cells in the Cu$_{2-x}$Se HNSs + 1064 nm group showed a large amount of red fluorescence, largely benefiting from the effective therapies and death mechanisms induced by enzymatic, photothermal, and photo-thermoelectric catalysis. To further quantify the ability to induce apoptosis, classical flow cytometry analysis with Annexin V-FITC and PI co-staining was performed (Fig. 7l and Supplementary Fig. 13c). Apoptotic cells were negligible in control and 1064 nm groups, while 1064 nm laser-activated Cu$_{2-x}$Se HNSs induced apoptosis up to 78.96% (sum of Q2 + Q3), which is much higher than that of the Cu$_{2-x}$Se HNSs treated group (≈50.64%). These in vitro results verified that the photothermal, enhanced enzymatic, and thermoelectric catalysis therapies of Cu$_{2-x}$Se HNSs evoked cuproptosis and apoptosis and as a result, achieved a highly synergistic treatment effect and triggered serious cell death.

In vivo therapeutic effect

Encouraged by the promising cell-killing ability in vitro, we next sought to determine whether Cu$_{2-x}$Se HNSs under 1064 nm irradiation are effective against tumors in vivo. Therefore, we established a CT26 tumor-bearing mouse model (Fig. 8a). Twenty female BALB/$_C$ mice were randomly divided into four treated groups: (1) control, (2) 1064 nm, (3) Cu$_{2-x}$Se HNSs, and (4) Cu$_{2-x}$Se HNSs + 1064 nm. Mice in groups (3) and (4) were injected with a Cu$_{2-x}$Se HNSs solution at a dosage of 2 mg kg^{-1} by tail vein injection, and mice in groups (2) and (4) were exposed to a 1064 nm laser (1.0 W cm^{-2}, 5 min) for several durations. The tumor volume and body weight were measured every two days. Inductively coupled plasma-mass spectrometry (ICP-MS) was used to determine the pharmacokinetic profile of Cu$_{2-x}$Se HNSs in mice at different time intervals (Fig. 8b). It can be observed that in the liver, spleen, lung, and kidney, the Cu content remained high during the first 12 h, and then Cu began to be metabolized out of the body over time, preventing possible toxic side effects caused by retention of the raw material in the body. The effective accumulation of Cu$_{2-x}$Se HNSs in the tumor was consistently high, reaching a maximum of 9.03% ID g^{-1} of tissue after 12 h, suitable for causing cuproptosis. Subsequently, we analyzed the pharmacokinetics in blood using a two-compartment model, as shown in Supplementary Fig. 14a. The elimination half-life of 0.11 h ensures low toxicity to the organism, while the terminal half-life of 6.74 h ensures the efficacy of the nanomedicine. Prior to the in vivo experiments, we examined the effect of Cu$_{2-x}$Se HNSs on mouse venous blood using a hemolysis assay (Fig. 8c and
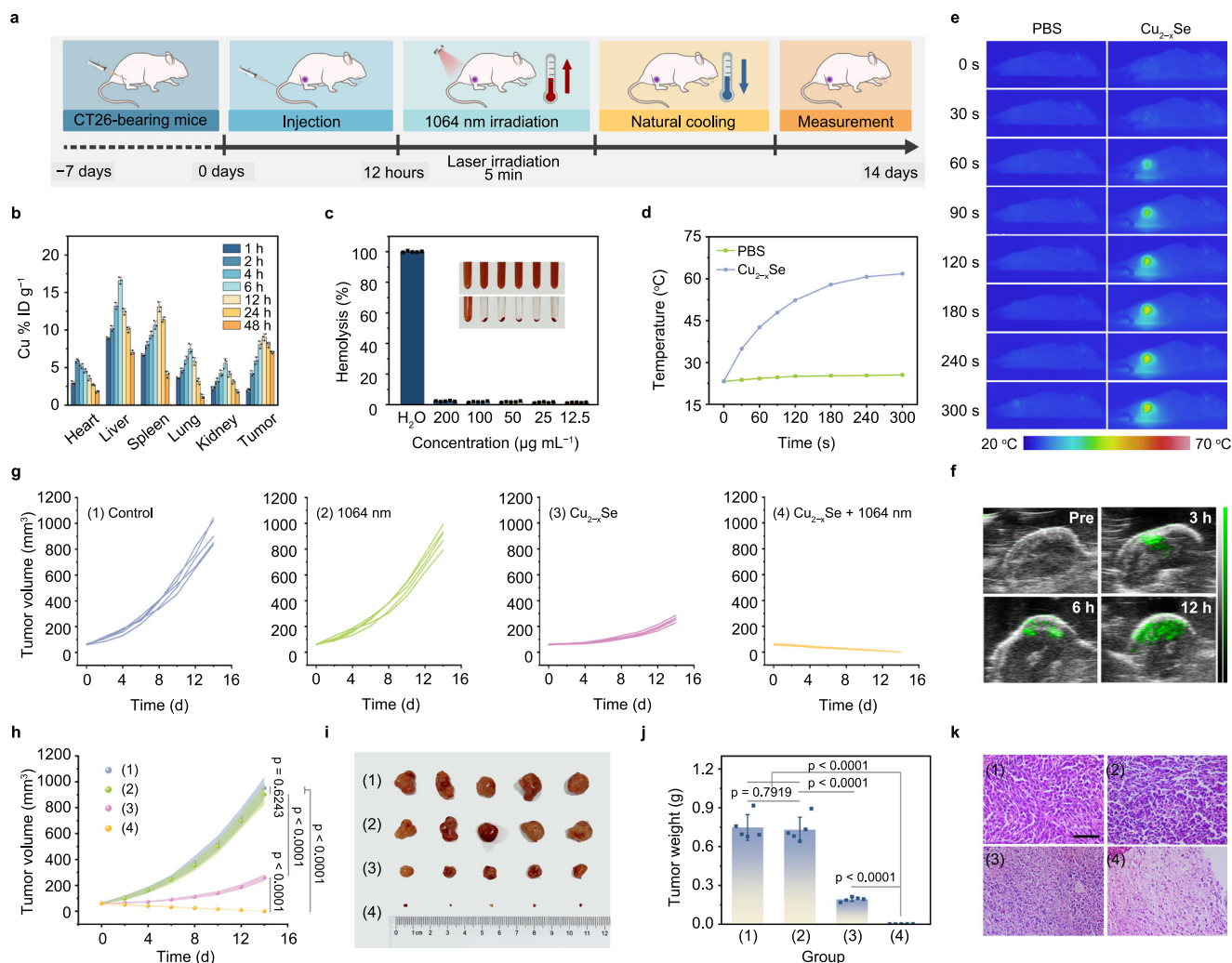
Fig. 8 | In vivo anti-tumor effect in BALB/c mice. a Therapeutic schedule of Cu$_{2-x}$Se HNSs for CT26 tumor-bearing mice. **b** Biodistribution of Cu in major organs and tumors after tail vein injection of Cu$_{2-x}$Se HNSs solution at different time intervals (% injectable dose (ID) of Cu per gram of tissue, $n = 3$ biologically independent samples). **c** Assessment of hemolysis of erythrocytes by Cu$_{2-x}$Se HNSs in distilled water (DW) ($n = 5$ biologically independent data). **d**–**e** Tumor temperature change curves (**d**) and corresponding infrared thermal images (**e**)

obtained under 1064 nm irradiation after injection of PBS and Cu$_{2-x}$Se HNSs in mice. **f** The PA images of the tumor area after tail vein injection of Cu$_{2-x}$Se HNSs at different time points. **g**–**k** Tumor volume (**g**, **h**), a photograph of the dissected tumor (**i**), tumor weight (**j**), and H&E-stained photographs of tumor slices after various treatments (**k**). Scale bar for **k**: 50 μm. Data presented as mean ± S.D. ($n = 5$ mice). Source data are provided as a Source Data file.

Supplementary Fig. 14b). The phenomenon of red supernatants induced by erythrocyte lysis was negligible in all experimental groups, suggesting no adverse effects of Cu$_{2-x}$Se HNSs on the blood.

Next, real-time thermal imaging images of mice injected with Cu$_{2-x}$Se HNSs and exposed to 1064 nm radiation (1.0 W cm^{-2}, 5 min) were taken on a thermal imaging camera. Temperature variation curves (Fig. 8d) were drawn based on the thermal imaging images of the mice (Fig. 8e). The tumor temperature on the epidermis for the Cu$_{2-x}$Se HNSs + laser group was positively correlated with time, typically, remarkably increased from 23.2 °C to 61.8 °C in 5 min. This is due to the photothermal properties of Cu$_{2-x}$Se HNSs, which produce an effective and fast heating rate under 1064 nm excitation. However, the tumor epidermis of mice injected with PBS had a stable temperature variation of about 2.4 °C under the laser. The excellent NIR-II excited photothermal performance makes Cu$_{2-x}$Se HNSs good for tumor-specific photoacoustic (PA) imaging. The Vevo LAZR-X system was used to record the PA images of Cu$_{2-x}$Se HNSs. First, the PA images and corresponding signal intensity of Cu$_{2-x}$Se HNSs solutions with different concentrations were characterized (Supplementary Fig. 15a, b). As the concentration of Cu$_{2-x}$Se HNSs was increased, the PA signal

intensity showed a linear correlation, indicating the potential to achieve PA imaging in vivo. Afterward, Cu$_{2-x}$Se HNSs were injected into CT 26-bearing mice *via* the tail vein, and the PA images of tumor sites were taken (shown in Fig. 8f and Supplementary Fig. 15c). As shown, significant signal intensity started to be observed at the tumor within 3 h. With increasing time, the signal intensity was gradually increased with a time-dependent pattern. The strongest signal intensity was observed at 12 h, while the signal almost disappeared at 24 h. These results suggest that Cu$_{2-x}$Se HNSs are a good PA contrast agent for tumor detection.

Finally, the change in the tumor volume of each mouse during the 14 days of treatment was recorded (Fig. 8g), and the average tumor volume of each group was derived (Fig. 8h). The tumor growth rate of the control group was rapid, and the tumor volume of the 1064 nm group did not show effective growth inhibition. However, the mice in the Cu$_{2-x}$Se HNSs group showed an obvious tumor inhibition effect, and the tumors in the Cu$_{2-x}$Se HNSs + 1064 nm group were almost removed completely within 8 days, which can be attributed to the effective therapeutic effect of photothermal, enzymatic, and thermoelectric catalysis, as well as the induced cell death mechanisms of

cuproptosis and apoptosis. After 14 days of treatment, digital photographs of dissected tumors were taken for all treated mice (Fig. 8i), and the tumors were weighed to compare the treatment effects (Fig. 8j). Supplementary Fig. 16 shows the changes in the body weight of the mice after treatment. No apparent weight fluctuations were observed in any mouse, confirming that the treatments had no significant adverse effects on the survival status of the mice. Figure 8k and Supplementary Fig. 17 show the H&E staining of the tumor and major organ sections obtained after treatment. For the tumor tissue sections, no significant damage was observed in the control and 1064 nm groups, yet local damage was observed in the $Cu_{2-x}Se$ HNSs group; specifically, a distinct cell death was evidenced in the $Cu_{2-x}Se$ HNSs + 1064 nm group. No morphological changes were observed in tissue sections of other major organs, demonstrating safety. From the above hematological and histological analyses, it can be concluded that $Cu_{2-x}Se$ HNSs activated by 1064 nm radiation achieve effective tumor suppression through synergistic photothermal, enzymatic, and thermoelectric catalysis, as well as the induced cell death mechanisms of cuproptosis and apoptosis in mice. Furthermore, we simulated the clinical application of $Cu_{2-x}Se$ HNSs using an in situ colon cancer mouse model. The 1064 nm-activated $Cu_{2-x}Se$ HNSs also demonstrated good efficacy against in situ colon cancer, as evidenced by the tumor bioluminescence in Supplementary Fig. 18.

Discussion

Inspiration from the photo-thermoelectric effect, heat can also be used as energy input and thermoelectric materials can be used to convert thermal energy into electrical energy and promote the production of ROS to induce tumor cell apoptosis. Accordingly, we present urchin-like $Cu_{2-x}Se$ HNSs by taking advantage of the Kirkendall effect, which was applied for photothermal, thermal-enhanced enzymatic, and plasmonic-thermoelectric synergistic therapy. Without laser irradiation, $Cu_{2-x}Se$ HNSs nanozyme possesses both POD- and CAT-like activities, which could catalyze H_2O_2 to ·OH for enzymatic therapy and catalyze H_2O_2 to O_2 as raw material for combined therapy. The V_{max} and K_m were determined to be $2.57 \times 10^{-8}\,M\,s^{-1}$ and 30.01 mM, respectively, for $Cu_{2-x}Se$ HNSs at RT. DFT calculations proved that after the formation of defects, charge redistribution and the higher oxidation state of the active sites will facilitate the oxidation of H_2O_2 to form O_2, being favorable for the much more improved catalytic activity of the material.

Excitingly, under a 1064 nm laser, the excellent plasmonic photothermal performance of $Cu_{2-x}Se$ HNSs was obtained due to the high η of ~67.0%. Large amounts of ROS will be generated due to the photothermal enhanced POD-like activity and thermoelectric catalysis performance of $Cu_{2-x}Se$ HNSs. Because when $Cu_{2-x}Se$ HNSs are illuminated by light, the local temperature will increase under the action of the photothermal effect. The temperature gradient inside the material drives the diffusion of charge carriers from the hot end to the cold end, thereby establishing a potential difference. Both in vitro and in vivo experiments proved the sharply increased ROS generation by heating/cooling cycles. This behavior is attributed to the enduring plasmonic photothermal capabilities of $Cu_{2-x}Se$ HNSs, which maintain the ability to facilitate the separation of e^- and h^+ for cascade catalytic reactions. Accordingly, the energy conversion path of photothermal effect, thermoelectricity, and ROS have been revealed, which showed a more significant catalytic activity than the enzymatic catalysis activities of $Cu_{2-x}Se$ HNSs. DFT calculations further proved that the presence of V_{Cu} contributed to the enhancement of the carrier concentration and electron conductivity while achieving Cu ion-free diffusion to form polarization changes. When used in cancer therapy, both cell cuproptosis and apoptosis are activated by ROS, heat, and Cu accumulation, thereby exhibiting efficient treatment performance in vivo. Our study provides a simple approach for energy-converting nanomedicines for tumor therapy by activating the cell death pathway.

Moreover, this work is important in the design, preparation, mechanism breakthrough, and efficacy evaluation of thermal-based anticancer therapeutic agents, expanding biomedical research, and developing therapeutic paths.

Methods

Ethical statement

Female BALB/c mice (four weeks old) were purchased from Beijing Vital River Laboratory Animal Technology Co. Ltd. (Beijing, China; 1100111084356). The mice were housed at a temperature of 23–25 °C and $50.0 \pm 5.0\%$ humidity environment with free access to food and water in a 12 h light/dark cycle. All animal experiments were approved by the Ethics Committee of the Second Affiliated Hospital of Harbin Medical University (Harbin, China). All animal experiments were performed in accordance with the Guidelines for the Care and Use of Laboratory Animals of the Drug Safety Evaluation Center of Harbin Medical University (No. GZRDW2022-001). The institution did not allow mice to have tumors larger than 17 mm in diameter or more than 1700 mm^3 in volume. In this experiment, none of the tumor volumes exceed the maximal tumor size/burden.

Synthesis of Cu_2O NPs

Cu_2O NPs were prepared and used as sacrificial templates. Briefly, 0.576 g of sodium dodecyl sulfate (SDS) was dissolved in 81 mL of deionized water and stirred for 10 min. Subsequently, 1 mL of $CuSO_4$ (0.1 mol L^{-1}) was added, and the mixture was stirred for 5 min. Next, NaOH solution (1 mol L^{-1}, 0.9 mL) was quickly added. After 30 s, 17 mL of sodium ascorbate was added, stirred for another 5 min, and aged for 10 min. The Cu_2O NPs were then obtained by centrifugation ($21380 \times g$, 5 min) and washed three times with deionized water and ethanol.

Synthesis of $Cu_{2-x}Se$ HNSs

The $Cu_{2-x}Se$ HNSs were prepared by a template-directed method. First, 15.79 mg of Se powder and 30.26 mg of $NaBH_4$ were placed in a three-necked flask, which was sealed with nitrogen gas. Next, 5 mL of deionized water was poured into the flask, and the solution was stirred for 1.5 h. Then, 30 mL of the Cu_2O dispersion was added to the three-necked flask. The obtained mixture was stirred for another 2 h. Finally, the $Cu_{2-x}Se$ HNSs were obtained by centrifugation ($21380 \times g$, 5 min) and washed three times.

In Vitro Photothermal Performance

$Cu_{2-x}Se$ HNSs dispersions with different concentrations were illuminated with a 1064 nm laser for 300 s. Temperature variation over time was photographed using an infrared thermal camera (FLIR System E40). Using a similar method, the relationship between the irradiation time and laser power was recorded. To characterize the photothermal stability, a $Cu_{2-x}Se$ HNSs dispersion was irradiated upon a 1064 nm laser with the power density of 1 W cm^{-2} for 300 s, then cooled to RT naturally. The heating and cooling processes were recorded over five cycles.

In Vitro POD-like activity and kinetic analysis

To analyze the POD-like activity, a mixture solution was prepared in 3 mL PBS (pH 5.5) with TMB as substrate and $Cu_{2-x}Se$ HNSs (80 μg mL^{-1}) as a catalyst in the presence of H_2O_2. The TMB solution was firstly prepared by dissolving 1 mg of TMB in 100 μL of dimethyl sulfoxide (DMSO), and then adding distilled water to 1 mL. Each 3 mL of the solution to be tested contained 100 μL of the TMB solution. The POD-like activity of $Cu_{2-x}Se$ HNSs was analyzed by using different concentrations of H_2O_2 as the substrate, monitoring the absorbance after different reaction times, and calculating the Michaelis-Menten constant from the saturation curve. Subsequently, the absorption spectra of the oxTMB in $Cu_{2-x}Se$ HNSs solution (80 μg mL^{-1}) were recorded by UV-vis spectrophotometry after certain time intervals. Meanwhile, the

absorption spectra of oxTMB in $Cu_{2-x}Se$ HNSs solution ($40\,\mu g\,mL^{-1}$) were obtained by fixing the reaction time at 5 min under the above conditions and controlling solution temperatures at RT, 40, and 60 °C.

Assessment of $^1O_2$ generation capacity

The $^1O_2$ generation capacity is an important indicator for evaluating the thermoelectric performance; therefore, a detailed characterization with DPBF as a substrate was conducted. First, the UV-vis spectra of DPBF in H_2O_2 and $Cu_{2-x}Se$ HNSs solution ($80\,\mu g\,mL^{-1}$, pH 5.5) after ascending to different temperature differences for 5 min were recorded by UV-vis spectrophotometer. Second, the above solution was placed in temperature fluctuation conditions by heating in a 60 °C water bath and then cooling in a 15 °C ice bath for 5 cycles. The UV-vis spectra of DPBF under temperature fluctuations were also recorded. Third, the above solution was placed in temperature fluctuation condition by 1064 nm irradiation for 5 min and cooling to 15 °C as a cycle. The UV-vis spectra were obtained over five cycles. Finally, the UV-vis spectra of the DPBF solution at pH 7.4 under the conditions of 60/15 °C + H_2O_2, RT + $Cu_{2-x}Se$ HNSs + H_2O_2, 60/15 °C + $Cu_{2-x}Se$ HNSs, 1064 nm + $Cu_{2-x}Se$ HNSs + H_2O_2, and 60/15 °C + $Cu_{2-x}Se$ HNSs + H_2O_2 were recorded for comparison.

Electrochemical measurements

Electrochemical impedance, current, and Mott-Schottky plot of $Cu_{2-x}Se$ HNSs were performed using an electrochemical workstation (CHI660E) in a 0.5 M Na_2SO_4 electrolyte. The experimental setup comprised Ag/AgCl reference electrodes and platinum electrodes. Subsequently, 20 μL of $Cu_{2-x}Se$ HNSs suspension was deposited onto the working electrode for measurement purposes. Notably, thermo-electric current measurements were conducted under cyclic conditions, involving heating in a 60 °C water bath and cooling in a 15 °C ice bath.

Western blot assays

CT26 cells (cell counts about 3×10^5 / well) were pre-incubated in 6-well plates. When cell density reached approximately 70−80 %, the cells were categorized into four groups and treated with (1) control, (2) 1064 nm, (3) $Cu_{2-x}Se$ HNSs, and (4) $Cu_{2-x}Se$ HNSs + 1064 nm. CT26 cells were lysed three times with RIPA lysis buffer (Beyotime, P0013B) containing protease inhibitor cocktail (Sigma-Aldrich, 05892970001) on ice for 10 min. Protein abundance was quantified by the bicinchoninic acid protein assay kit (Beyotime, P0012) and using a bovine-specific albumin standard curve for normalization of protein abundance. Then, 20- 40 μg of each sample was fractionated by SDS polyacrylamide gels in SDS running buffer and transferred to polyvinylidene fluoride membranes (Sigma-Aldrich, 03010040001). After blocking with 5% non-fat dry milk (Cell Signaling Technology, 9999) at RT for 1 h, the membranes were incubated with primary antibodies LIAS (Proteintech, Cat# 11577-1-AP), FDX1 (Abcam, Cat# ab108257), active Bax (Santa Cruz Biotechnology, Cat# sc-23959), total Bax (Abcam, Cat# ab3191), Casp-3 (Abcam, Cat# ab182734), C-Casp-3 (Cell Signaling Technology, Cat# 9661s), and DLAT (Proteintech, Cat# 13426-1-AP) overnight at 4 °C. After washing with TBST, the membranes were incubated with the fluorophore-specific secondary antibody at room temperature for 1 h and washed with TBST. Finally, the protein signal was visualized using the LI-COR Odyssey® CLx Imaging Systems. Quantitative analysis of protein expression was performed using LI-COR Image Studio™ Software.

In vivo assessment of the therapeutic effect

A total of twenty mice, each bearing tumors with a size of 60 mm³, were segregated into the following treatment cohorts: (1) control, (2) 1064 nm, (3) $Cu_{2-x}Se$ HNSs, (4) $Cu_{2-x}Se$ HNSs + 1064 nm. Typically, mice in groups (3) and (4) were injected with 100 μL of $Cu_{2-x}Se$ HNSs solution ($10\,mg\,kg^{-1}$) *via* the tail vein. The mice in groups (3) and (4)

were then irradiated with 1064 nm light at certain time points. Following this, the tumor volume and body weight of the mice were measured every two days to evaluate the treatment's effectiveness. After 14 days of treatment, the major organs and tumors were excised, photographed, and subjected to staining with hematoxylin and eosin for histological examination. The therapeutic effect was also evaluated using the orthotopic tumor model. Female BALB/c mice were anes-thetized with isoflurane inhalation, and the cecum was exposed *via* a lower abdominal incision. Then, ~ 2×10^5 luciferase reporter expressing CT26 (CT26-Luc) cells in 50 μL of PBS were injected subserosally using an insulin syringe (30G) under the microscope. After 3 days of tumor growth, various above-mentioned treatments were initiated (Day 0). Mice were monitored every 5 days by an in vivo imaging system (IVIS) following intraperitoneal administration of D-Luciferin.

Statistics and reproducibility. All experiments were independently performed at least three times. Quantitative data were presented as mean ± standard deviation (mean ± SD). Analysis of variance (ANOVA) was used for multiple comparisons, and the student's unpaired *t* test (two-tailed) was used for two-group comparisons. *p* values < 0.05 were considered statistically significant. All cells and the animals were ran-domly allocated to experimental groups. The investigators were blin-ded to allocation during experiments and outcome assessment.

Reporting summary

Further information on research design is available in the Nature Portfolio Reporting Summary linked to this article.

Data availability

All the data generated and analyzed from this study are presented in the article and its Supplementary Information files. The data are also available from the corresponding author upon request. Source data are provided in this paper.

References

1. Wang, S. et al. Reduced graphene oxides modified Bi_2Te_3 nanosh-eets for rapid photo-thermoelectric catalytic therapy of bacteria-infected wounds. *Adv. Funct. Mater.* **33**, 2210098 (2023).
2. Jiang, X. et al. A photo-activated thermoelectric catalyst for fer-roptosis-/pyroptosis-boosted tumor nanotherapy. *Adv. Healthc. Mater.* **12**, 2300699 (2023).
3. Liu, D. et al. Lattice plainification advances highly effective SnSe crystalline thermoelectrics. *Science* **380**, 841–846 (2023).
4. Hu, B. et al. Thermoelectrics for medical applications: progress, challenges, and perspectives. *Chem. Eng. J.* **437**, 135268 (2022).
5. Zhou, H. et al. Advancement of electrochemical thermoelectric conversion with molecular technology. *Angew. Chem. Int. Ed.* **62**, 2213449 (2023).
6. Ji, X. et al. Nanoheterojunction-mediated thermoelectric strategy for cancer surgical adjuvant treatment and β-elemene combination therapy. *Adv. Mater.* **35**, 2207391 (2023).
7. Kang, Y. et al. A Novel cascaded energy conversion system indu-cing efficient and precise cancer therapy. *Bioact. Mater.* **20**, 663–676 (2023).
8. You, H. et al. Accelerated pyro-catalytic hydrogen production enabled by plasmonic local heating of Au on pyroelectric $BaTiO_3$ nanoparticles. *Nat. Commun.* **13**, 6144 (2022).
9. Horide, T. et al. Thermoelectric property in orthorhombic-domained SnSe film. *ACS Appl. Mater. Interfaces* **11**, 27057–27063 (2019).
10. He, W. et al. temperature gradient characteristics and effect on optimal thermoelectric performance in exhaust power-generation systems. *Appl. Energy* **261**, 114366 (2020).
11. Yuan, X. et al. Self-triggered thermoelectric nanoheterojunc-tion for cancer catalytic and immunotherapy. *Nat. Commun.* **14**, 5140 (2023).

12. Zang, P. et al. Photothermal-actuated thermoelectric therapy by harnessing janus-structured Ag-Ag$_2$S nanoparticles with enhanced antitumor efficacy. *Chem. Mater.* **35**, 7770–7780 (2023).

13. Curtis, B. J. et al. Cross-species transcriptomic signatures identify mechanisms related to species sensitivity and common responses to nanomaterials. *Nat. Nanotech.* **17**, 661–669 (2022).

14. Contini, C. et al. Size dependency of gold nanoparticles interacting with model membranes. *Commun. Chem.* **3**, 130 (2020).

15. Liu, Y. et al. Toxicity of manufactured nanomaterials. *Particuology* **69**, 31–48 (2022).

16. Kubo, W. et al. Quantitative analysis of the plasmonic photo-thermoelectric phenomenon. *J. Phys. Chem. C.* **123**, 21670–21675 (2019).

17. Ghorai, N. et al. Harvesting plasmonic near-infrared photons by hot hole transfer in nonstoichiometric-semiconductor plasmonic heterojunctions. *ACS Photonics* **10**, 733–742 (2023).

18. Zhang, Z. et al. A nonmetal plasmonic z-scheme photocatalyst with UV- to NIR-driven photocatalytic protons reduction. *Adv. Mater.* **29**, 1606688 (2017).

19. Ghorai, N. et al. Ultrafast plasmon dynamics and hole-phonon coupling in NIR active nonstoichiometric semiconductor plasmonic Cu$_{2-x}$S nanocrystals. *J. Phys. Chem. C* **123**, 28401–28410 (2019).

20. Jauffred, L. et al. Plasmonic heating of nanostructures. *Chem. Rev.* **119**, 8087–8130 (2019).

21. Li, F. et al. Plasmonic local heating induced strain modulation for enhanced efficiency and stability of perovskite solar cells. *Adv. Energy Mater.* **12**, 2200186 (2022).

22. Jeon, C.-Y. et al. Plasmon-enhanced photodetection in ferro-magnet/nonmagnet spin thermoelectric structures. *Adv. Funct. Mater.* **28**, 1802936 (2018).

23. Lin, L. et al. Opto-thermoelectric nanotweezers. *Nat. Photonics* **12**, 195–201 (2018).

24. Mauser, K. W. et al. Resonant thermoelectric nanophotonics. *Nat. Nanotechnol.* **12**, 770–775 (2017).

25. Hu, Y. et al. Mid-infrared circular-polarization-sensitive photo-detector based on a chiral metasurface with a photothermoelectric effect. *Appl. Opt.* **62**, 2292–2299 (2023).

26. De Trizio, L. et al. Cu$_{3-x}$P nanocrystals as a material platform for near-infrared plasmonics and cation exchange reactions. *Chem. Mater.* **27**, 1120–1128 (2015).

27. Zhao, H. et al. A self-independent binary-sublattice construction in Cu$_2$Se thermoelectric materials. *Adv. Funct. Mater.* **33**, 2304663 (2023).

28. Zhou, Z. et al. Compositing effects for high thermoelectric performance of Cu$_2$Se-based materials. *Nat. Commun.* **14**, 2410 (2023).

29. Shan, B. et al. High-quality dual-plasmonic Au@Cu$_{2-x}$Se nanocrescents with precise Cu$_{2-x}$Se domain size control and tunable optical properties in the second near-infrared biowindow. *Chem. Mater.* **31**, 9875–9886 (2019).

30. Ali, M. A. et al. Self-confined precipitation of ultrasmall plasmonic Cu$_{2-x}$Se particles in transparent solid medium. *J. Phys. Chem. C* **123**, 9394–9399 (2019).

31. Wang, X. et al. Ultrasensitive and broadband MoS$_2$ photodetector driven by ferroelectrics. *Adv. Mater.* **27**, 6575–6581 (2015).

32. Wu, K., Chen, J., McBride, J. R. & Lian, T. Efficient hot-electron transfer by a plasmon-induced interfacial charge-transfer transition. *Science* **349**, 632–635 (2015).

33. Cao, L. et al. Semiconductor nanowire optical antenna solar absorbers. *Nano Lett.* **10**, 439–445 (2010).

34. Li, M. et al. Near-infrared-II fluorophore with inverted dependence of fluorescence quantum yield on polarity as potent photo-theranostics for fluorescence image-guided phototherapy of tumors. **35**, *Adv. Mater.* e2209647 (2023).

35. Sun, P. et al. Peptide-mediated aqueous synthesis of NIR-II emitting Ag$_2$S quantum dots for rapid photocatalytic bacteria disinfection. *Angew. Chem. Int. Ed.* **62**, e2023000 (2023).

36. Feng, Z. et al. Engineered NIR-II fluorophores with ultralong-distance molecular packing for high-contrast deep lesion identification. *Nat. Commun.* **14**, 5017 (2023).

37. Liu, G. et al. Mo$_2$C-derived polyoxometalate for NIR-II photoacoustic imaging-guided chemodynamic/photothermal synergistic therapy. *Angew. Chem. Int. Ed.* **58**, 18641–18646 (2019).

38. Tsvetkov, P. et al. Copper induces cell death by targeting lipoylated TCA cycle proteins. *Science* **375**, 1254–1261 (2022).

39. Chan, L. et al. Cuproptosis-driven enhancement of thermotherapy by sequentially response Cu$_2$$_{-x}$Se via copper chemical transition. *Adv. Funct. Mater.* **33**, 2302054 (2023).

40. Ouyang, J. et al. Oral hydrogel microbeads-mediated in situ synthesis of selenoproteins for regulating intestinal immunity and microbiota. *J. Am. Chem. Soc.* **145**, 12193–12205 (2023).

41. Chang, Y. et al. Precise engineering of a Se/Te nanochaperone for reinvigorating cancer radio-immunotherapy. *Adv. Mater.* **35**, 2212178 (2023).

42. Huang, Y. et al. Chirality-driven transportation and oxidation prevention by chiral selenium nanoparticles. *Angew. Chem. Int. Ed.* **59**, 4406–4414 (2020).

43. Zhang, S. et al. Ambient aqueous synthesis of ultrasmall pegylated Cu$_{2-x}$Se nanoparticles as a multifunctional theranostic agent for multimodal imaging guided photothermal therapy of cancer. *Adv. Mater.* **28**, 8927–8936 (2016).

44. Ji, C. et al. A nano vector with photothermally enhanced drug release and retention to overcome cancer multidrug resistance. *Nano Today* **36**, 101020 (2021).

45. Yuan, J. et al. Controlled activation of TRPV1 channels on microglia to boost their autophagy for clearance of alpha-synuclein and enhance therapy of parkinson's disease. *Adv. Mater.* **34**, 2108435 (2022).

46. Phillips, R. Urchin-like nanoparticles for miRNA therapy of OA. *Nat. Rev. Rheumatol.* **19**, 537 (2023).

47. Zhao, J. et al. Insights into the effect of catalytic intratumoral lactate depletion on metabolic reprogramming and immune activation for antitumoral activity. *Adv. Sci.* **10**, 2204808 (2023).

48. Chen, H. et al. Urchin-like ceria nanoparticles for enhanced gene therapy of osteoarthritis. *Sci. Adv.* **9**, eadf0988 (2023).

49. Wang, X. et al. Hollow Cu$_2$Se nanozymes for tumor photothermal-catalytic therapy. *Chem. Mater.* **31**, 6174–6186 (2019).

50. Hussain, I. et al. Hollow nano- and microstructures: mechanism, composition, applications, and factors affecting morphology and performance. *Coord. Chem. Rev.* **458**, 214429 (2022).

51. Yang, C. et al. Heterostructural nanoadjuvant CuSe/CoSe$_2$ for potentiating ferroptosis and photoimmunotherapy through intratumoral blocked lactate efflux. *J. Am. Chem. Soc.* **145**, 7205–7217 (2023).

52. Ghorai, N. et al. Ultrafast plasmon dynamics in near-infrared active non-stoichiometric Cu$_{2-x}$Se nanocrystals and effect of chemical interface damping. *J. Phys. Chem. C* **125**, 11468–11477 (2021).

53. Pan, L. et al. Cascade catalytic nanoparticles selectively alkalize cancerous lysosomes to suppress cancer progression and metastasis. *Adv. Mater.* **36**, e2305394 (2023).

54. Chu, Z. et al. Recent Advances on modulation of H$_2$O$_2$ in tumor microenvironment for enhanced cancer therapeutic efficacy. *Coord. Chem. Rev.* **481**, 215049 (2023).

55. Wang, D. et al. Missing-linker-confined single-atomic Pt nanozymes for enzymatic theranostics of tumor. *Angew. Chem. Int. Ed.* **62**, e202217995 (2023).

56. Klan, J. M. et al. Theoretical study of the impact of vacancies and disorder on the electronic properties of Cu$_{2-x}$Se. *J. Phys. Chem. C.* **125**, 12324–12332 (2021).

57. Huang, Y. et al. Unconventional doping effect leads to ultrahigh average thermoelectric power factor in Cu_3SbSe_4-based composites. *Adv. Mater.* **34**, 109952 (2022).

58. Roychowdhury, S. et al. Stabilizing n-type cubic GeSe by entropy-driven alloying of $AgBiSe_2$: ultralow thermal conductivity and promising thermoelectric performance. *Angew. Chem. Int. Ed.* **57**, 15167–15171 (2018).

59. Norskov, J. K. et al. Towards the computational design of solid catalysts. *Nat. Chem.* **1**, 37–46 (2009).

60. Liu, H. et al. Copper ion liquid-like thermoelectrics. *Nat. Mater.* **11**, 422–425 (2012).

61. Madsen, G. K. H. et al. A code for calculating band-structure dependent quantities. *Comput. Phys. Commun.* **175**, 67–71 (2006).

62. Yang, L. et al. Impacts of Cu deficiency on the thermoelectric properties of $Cu_{2-x}Se$ nanoplates. *Acta Mater.* **113**, 140–146 (2016).

63. Liu, L. et al. The physiological metabolite α-ketoglutarate ameliorates osteoarthritis by regulating mitophagy and oxidative stress. *Redox Biol.* **62**, 102663 (2023).

64. Zhang, R. et al. Autophagy-activated self-reporting photosensitizer promoting cell mortality in cancer starvation therapy. *Adv. Sci.* **10**, 2301295 (2023).

65. Xia, Y. et al. Spatially confined intervention of cellular senescence by a lysosomal metabolism targeting molecular prodrug for broad-spectrum senotherapy. *Angew. Chem. Int. Ed.* **61**, e202115764 (2022).

66. Li, W. et al. Molecular engineering of pH-responsive NIR Oxazine assemblies for evoking tumor ferroptosis via triggering lysosomal dysfunction. *J. Am. Chem. Soc.* **145**, 3736–3747 (2023).

Acknowledgements

Author contributions

L.Y. and Z.Z. conceived the idea and designed the project. L.Y., Z.Z., and B.Z. performed the experiments and analyzed the results. B.T., Y.D., and S.G. assisted with the experiment design and data analyses. L.Y. wrote and revised the original draft of the manuscript. M.Y. and Y.X. performed the DFT calculations. J.L., Y.X., and S.G. reviewed and edited the manuscript. J.L. supervised the whole project. All authors discussed the results and commented on the manuscript.

Competing interests

The authors declare no competing interests.

Additional information

Supplementary information The online version contains supplementary material available at https://doi.org/10.1038/s41467-024-51772-1.

Correspondence and requests for materials should be addressed to Shili Gai, Ying Xie or Jun Lin.

Peer review information *Nature Communications* thanks Junjie Cheng, Xiaobin Zeng and the other anonymous, reviewer(s) for their contribution to the peer review of this work. A peer review file is available.

Reprints and permissions information is available at http://www.nature.com/reprints

Publisher's note Springer Nature remains neutral with regard to jurisdictional claims in published maps and institutional affiliations.

[1]Key Laboratory of Superlight Materials and Surface Technology, Ministry of Education, College of Material Sciences and Chemical Engineering, Harbin Engineering University, Harbin, P. R. China. [2]State Key Laboratory of Rare Resource Utilization, Changchun Institute of Applied Chemistry, Chinese Academy of Sciences, Changchun, P. R. China. [3]Department of Ultrasound, the First Affiliated Hospital of Harbin Medical University, Harbin, P. R. China. [4]Key Laboratory of Functional Inorganic Material Chemistry, Ministry of Education, School of Chemistry and Materials Science, Heilongjiang University, Harbin, P. R. China. [5]These authors contributed equally: Lu Yang, Zhiyu Zhao. ✉e-mail: gaishili@hrbeu.edu.cn; xieying@hlju.edu.cn; jlin@ciac.ac.cn